

**Nonlinear Receptivity and Instability Studies by Proper Orthogonal Decomposition**

Journal:	<i>2011 Hawaii Summer Conferences</i>
Manuscript ID:	Draft
IuMeetingID:	2225
Date Submitted by the Author:	n/a
Contact Author:	Sengupta, Tapan

SCHOLARONE™  
Manuscripts

# Nonlinear Receptivity and Instability Studies by Proper Orthogonal Decomposition

Tapan K. Sengupta,\*

Swagata Bhaumik<sup>†</sup> and Yogesh G. Bhumkar<sup>†</sup>

*Indian Institute of Technology Kanpur, Kanpur 208 016, INDIA*

Spatio-temporal receptivity and instability of different flows are studied using proper orthogonal decomposition (POD) with accurate solutions of Navier-Stokes equation. This is performed via dynamical system approach for global spatio-temporal nonlinear receptivity/instability of flows. In the presence of single dominant mode, instability and its saturation have been studied in the past using classical Stuart-Landau (SL) equation. Flows past a circular cylinder and in a square lid-driven cavity display presence of multiple modes and bifurcation sequences, in addition to certain universal features of POD and instability modes given in Sengupta *et al.* (Universal instability modes in external and external flows - Computers & Fluids, 40(1), 221 - 235 (2011)). POD modes have been classified into regular modes which satisfy SL equation and anomalous modes which do not do so. Further studies on nonlinear receptivities and instabilities for complex wall-bounded external flows past bluff and streamlined bodies experiencing different pressure gradients are reported here for different flow parameter combinations. We also report flow inside rectangular cavity (with 2:1, depth to width ratio), flow past a heated horizontal flat plates to investigate other categories of POD/ instability modes. Specifically, receptivity of a semi-infinite flat plate and nonlinear instabilities characterized by Kelvin-Helmholtz and bypass route of flow instabilities past a natural laminar flow aerofoil are reported and contrasted with other flows in this review.

## I. Introduction

Proper orthogonal decomposition (POD) was originally developed by Kosambi<sup>1</sup> for a random field ( $v_i(X, t)$ ), which projects itself onto a set of deterministic vector ( $\phi_i(X)$ ), so that  $\langle v_i \phi_i \rangle^2$  is maximized - with angular bracket representing time averaging operation. Subsequently, this has been utilized for stochastic fluid dynamical systems, as in turbulent fluid flow. In recent times, POD has been further developed to explain complex spatio-temporal dynamics of deterministic fluid flows, as during the flow instability stage. Choice of  $\phi_i$  in the above, are fixed from an optimization problem given by the equation<sup>2</sup>

$$\int_S R_{ij}(X, X') \phi_j(X') d^2 X' = \lambda \phi_i(X) \quad (1.1)$$

The kernel of this equation is the two-point correlation function,  $R_{ij} = \langle v_i(X)v_j(X') \rangle$  of the random field. For flows with finite energy, classical Hilbert-Schmidt theory applies to give rise to denumerably infinite POD modes which are orthogonal to each other. If one is studying disturbance quantities in instability theories, then the disturbance remains finite, even when one is investigating inhomogeneous flow of infinite extent. This is due to the fact that the disturbance field receives its energy from the equilibrium flow which has finite energy. Thus, many of the theoretical restrictions of using POD for turbulent flows related to the applicability of Hilbert-Schmidt theory are not present for flows suffering instability and transition.

POD as a tool to study fluid flows was initiated by Lumley<sup>3</sup> and co-authors to elucidate coherent structures in turbulent flows<sup>4</sup>. This was facilitated by the method of snapshots<sup>5,6</sup>. In recent times, it has been used as a reduced order model for unsteady laminar and transitional flows<sup>7,8</sup>. Based on accurate numerical

---

\*Professor, High Performance Computing Laboratory, Department of Aerospace Engineering.

<sup>†</sup>Graduate Student, High Performance Computing Laboratory, Department of Aerospace Engineering

simulations of Navier-Stokes equation, various types of POD modes were identified and cataloged showing presence of multiple Hopf bifurcations for the dominant modes<sup>8,9</sup> for flow past a circular cylinder. In Sengupta *et al.*<sup>9</sup>, this was extended to flow inside a lid-driven square cavity (LDC) and universal nature of POD/ instability modes were shown by comparing these modes for flow past a circular cylinder and flow inside a LDC.

Disturbance vorticity field is represented in POD formalism by<sup>8,9</sup>

$$\omega'(\mathbf{X}, t) = \sum_{m=1}^M a_m(t) \phi_m(\mathbf{X}) \quad (1.2)$$

The correlation function of Eq. (1.1) is thus obtained as

$$R_{ij} = (1/M) \int \int \omega'(\mathbf{X}, t_i) \omega'(\mathbf{X}', t_j) d^2 \mathbf{X}$$

with  $i, j = 1, 2, \dots, M$  defined over the snapshots of the domain.

For 2D and 3D flows past circular cylinder, application of POD are reported in the literature<sup>8,10-13</sup>. Nonlinear aspect of flow instability was studied<sup>8,9</sup> by relating POD and instability modes without any modeling. As emphasized earlier<sup>2</sup>, one can use POD of numerical solution to study dynamical system without any models provided the numerical results are highly accurate.

## II. Representative Flows Investigated for POD Analysis

In the following, we report some flows for which POD analysis is performed here. These include the canonical flows like those investigated in Sengupta *et al.*<sup>8,9</sup> for flow past a single circular cylinder and flow inside a square LDC. In Figure 1a, vorticity contours are shown for (i) flow past a single stationary cylinder for  $Re = U_\infty^* d^*/\nu = 150$  (top frame) - with  $d^*$  as the diameter of the cylinder and  $\nu$  is the kinematic viscosity; (ii) flow past two side-by-side stationary cylinders, when the gap to diameter ratio ( $s^*/d^*$ ) between the cylinders is 2.5 for  $Re = U_\infty^* d^*/\nu = 100$  (middle frame) solved by chimera grid method<sup>14</sup> and (iii) flow past a single cylinder executing rotary oscillation<sup>15</sup> for  $Re = 150$ , with the oscillation parameters defined by the instantaneous rotation rate ( $\Omega^*$ )

$$\Omega^* = \Omega_1^* \sin(2S_f t)$$

where the maximum rotation rate ( $\Omega_1^*$ ) is related to maximum angular excursion ( $\theta_r$ ) by  $\Omega_1^* = 2\pi f_f^* \theta_r$  with  $f_f^*$  as the forcing frequency, whose nondimensional form is given by  $S_f = f_f^* d^*/U_\infty^*$ . All quantities with asterisks denote dimensional values. Nondimensional surface speed ( $\tilde{a}$ ) is obtained as  $\tilde{a} = \Omega_1^* d^*/2U_\infty^*$  and this together with  $S_f$  are the major parameters defining the rotary oscillation of the cylinder. For the flow in the bottom frame, these two parameters used are given by,  $\tilde{a} = 2$  and  $S_f = \pi/2$ .

In Figure 1b, vorticity contours are shown for flow inside a square and rectangular (2 : 1 aspect ratio) LDCs for  $Re = 10000$  and  $6000$ , respectively, at the indicated times. Distinctive feature of this internal flow is the presence of polygonal core vortex, which was demonstrated in<sup>16,17</sup> obtained using the developed high accuracy combined compact difference scheme for the square LDC. This flow in square LDC was subsequently analyzed<sup>19</sup> using POD and the modes were qualitatively related to similar modes shown for flow past a single stationary cylinder<sup>8</sup>. Here, the same numerical method has been used to investigate the flow inside the rectangular LDC. This flow has been earlier studied<sup>18</sup>, with critical Reynolds number predicted incorrectly. Presented results here are to provide instability portrait of this flow which has not been studied very often. Despite seeming similarity of exciting the flow through the motion of the lid (from left to right), the two halves of the flow inside the rectangular cavity are dissimilar topologically. While the top half shows polygonal vortex in the core and a jet-like flow is seen from right to left along the center of the cavity which hits the left vertical wall. Ensuing motion creates a helical vortex thread that moves towards the center of the lower half, which is slightly lifted above the geometric center. This elongated vortical element suffers Kelvin-Helmholtz instability, exhibiting beads of vortices around the core.

Instability of flow past a semi-infinite plate is another canonical problem which is often studied in developing methods and physical model of transition phenomenon. We emphasize that the current state of art which tries to show equivalence of instability with transition process is an erroneous one. One of the major reasons, for undertaking the study of this problem is to show some of the recent advances by the authors'

group to track the transition process from the receptivity stage. Thus, one is interested in triggering instability of flow by deterministic excitation, as shown in the top frame of Figure 1c. Here the flow instability is triggered by a simultaneous blowing-suction (SBS) strip on the plate, near the leading edge - as shown in the top frame. Consider the strip to be placed between  $x_1$  and  $x_2$ , as shown in the schematic diagram (Figure 1c). Wall perturbation stream function value ( $\psi_{wp}$ ) can be obtained from no-slip condition and an expression for wall-normal velocity given respectively by

$$u_d = 0, \quad v_d = A_0(x) \sin(\beta_L t) \quad (2.1)$$

where  $\beta_L$  is the non-dimensional disturbance frequency based on length scale ( $L$ ) and  $A_0(x)$  is the amplitude of the disturbance velocity. The amplitude function,  $A_0(x)$  is related to  $A_m(x)$  as  $A_0(x) = \alpha_1 A_m(x)$ , where  $\alpha_1$  is the amplitude control parameter and  $A_m(x)$  is defined in reference<sup>19, 20</sup> as, for  $x_1 \leq x \leq x_{st}$ :

$$A_m = 15.1875 \left( \frac{x - x_1}{x_{st} - x_1} \right)^5 - 35.4375 \left( \frac{x - x_1}{x_{st} - x_1} \right)^4 + 20.25 \left( \frac{x - x_1}{x_{st} - x_1} \right)^3 \quad (2.2)$$

and for  $x_{st} \leq x \leq x_2$ :

$$A_m = -15.1875 \left( \frac{x_2 - x}{x_2 - x_{st}} \right)^5 + 35.4375 \left( \frac{x_2 - x}{x_2 - x_{st}} \right)^4 - 20.25 \left( \frac{x_2 - x}{x_2 - x_{st}} \right)^3 \quad (2.3)$$

where,  $x_{st} = (x_1 + x_2)/2$ . This excitation produces vortical disturbances which create experimentally observed downstream propagating waves in flows. Implication of the value of  $\alpha_1$  is in the magnitude of input disturbance amplitude. For example,  $\alpha_1 = 0.01$  implies an input harmonic disturbance amplitude to be 1% of the free stream speed.

For this instability problem, Reynolds number based on displacement thickness ( $Re_{\delta^*}$ ) and non-dimensional frequency of the exciter ( $\beta_0$ ) are the relevant parameters and the unstable region is within the loop shown in the bottom frame of Figure 1c. By definition, a constant physical frequency disturbance is marked by a ray given by,  $F = \beta_0/Re_{\delta^*}$ . The parameter  $F$  is related to the physical frequency  $f$  in Hz by  $F = 2\pi\nu f/U_\infty^2$ . It has been assumed traditionally that an output TS wave corresponding to a constant frequency input, locally adjusts itself to wave properties, as given by the solution of Orr-Sommerfeld equation. Boundary of the unstable region is the neutral curve and outside it, TS waves decay. The neutral curve of Figure 1c is considered very important in instability studies, which can also be obtained by linear receptivity approach, as solution of linearized Navier-Stokes equation in spectral plane for fixed frequency excitation, as reported earlier<sup>21, 22</sup>. Theoretically predicted neutral curve<sup>23, 24</sup> were verified experimentally<sup>25</sup>, by vibrating a ribbon at a fixed frequency, placed inside a boundary layer. Having established the onset of instability via TS waves, it has been ever since believed that such wavy disturbances are responsible for transition to turbulence, when the background disturbances are low. Early experiments<sup>25</sup> validated linear stability analysis applied to a viscous flow, yet it did not elucidate the complete process of transition, as described here. We show disturbances from receptivity to intermittent turbulent stage via an accurate simulation of 2D Navier-Stokes equation.

When the harmonic exciter is started impulsively, the flow field in due course of time displays three components, as shown in Figure 1d for two amplitudes of excitation ( $\alpha_1 = 0.0002$  and  $0.01$ ) for streamwise disturbance velocity component ( $u_d$ ). It has been shown<sup>26, 27</sup> that such excitation gives rise to a spatio-temporal wave front, which is apart from the asymptotic TS wave-packet shown earlier<sup>19, 20</sup>. We also note that apart from this, one observes the local solution<sup>28</sup>, in the immediate neighborhood of the exciter. It has been established that the local solution is a consequence of Tauber's theorem<sup>28</sup>, as applicable to the Fourier-Laplace transform of the disturbance quantities created by very localized disturbance sources. In the top two frames of Figure 1d, streamwise disturbance velocity is shown at the indicated times as a function of  $x$ , for a height of  $y = 11.33\delta_{ex}$ , for the amplitude control parameter,  $\alpha_1 = 0.0002$  and the nondimensional frequency of  $F = 10^{-4}$ . For this low amplitude of excitation, one notes all the three components with the local and asymptotic part of the disturbance virtually remaining stationary in space. In contrast, the spatio-temporal front convects to the right with time, while the amplitude keeps growing. This growth of the wave front is not unlimited, as it saturates due to nonlinear actions of bypass transition showing unsteady separation, which dominates over the TS wave-packet. Detailed dynamics of the disturbance front for this receptivity problem will be explained elsewhere. In the bottom two frames of Figure 1d, results for a higher amplitude of excitation,  $\alpha_1 = 0.01$  are shown for the indicated times. At  $t = 94$ , one can clearly see the three components of the solution, showing some minor differences between the linear instability theory with

nonlinear receptivity calculations. Once again, the dynamics of the wave front is important, as shown in the frame at  $t = 194$ , which shows the leading front to saturate nonlinearly via the bypass route with unsteady separation. In this frame, action of the front marked as  $A$  in spawning an upstream structure at  $B$  is interesting. Such upstream propagating events are very common with bypass transition and clearly indicate the pitfall of parabolized stability equation (PSE) as a tool for such events. PSE has been used in recent years, without ascertaining the actual dynamics of all transitional flows.

Flows become more complex, when heat transfer effects are added for the canonical instability problem of semi-infinite plate. In the presented results here, we confine our attention to the flow above a heated plate, for which the heat transfer effects are modeled using Boussinesq assumption. Details of the equilibrium flow and its instability portrait are given in Unnikrishnan<sup>29</sup> for different excitation amplitude for the same SBS strip exciter used on the plate, near the leading edge. The equilibrium flow is given by the Schneider's<sup>30</sup> profile in terms of a buoyancy parameter,  $K$ . In Figure 1e, streamwise disturbance velocity component is shown as a function of space for  $K = 3 \times 10^{-3}$  at the indicated height for two different amplitudes and frequencies of excitation. On the top two frames,  $u_d$  is plotted as function of  $x$ , for a very low amplitude of excitation ( $\alpha_1 = 0.0002$ ) where one can note distinct presence of TS wave-packet and the leading spatio-temporal wave front. When the amplitude control parameter of excitation is increased to  $\alpha_1 = 0.01$ , flow shows unsteady separation right from the location of local solution, while a front develops (as noted at  $t = 10$ ). Result shown at  $t = 90$  shows an interesting aspect of the transitional flow. In the range where the flow is linearly unstable, as indicated by two vertical dotted lines (in all the frames), in the first part one notes the presence of small wave-length disturbance field, typical of TS wave-packet and this is followed by larger wave-length events which distinctly show nonlinear effects and flow separation. Right at the leading edge of the front, flow is intermittent.

Finally, we show in Figure 1f, flow developing over a natural laminar flow aerofoil operating for  $Re = 10.3 \times 10^6$ , at zero angle of attack. By design, it should not exhibit turbulence in the major part of the shear layer forming over the aerofoil. For this reason, the flow has been computed here utilizing a  $(5169 \times 577)$  grid. In the top frame of Figure 1f, some representative streamlines are drawn over the aerofoil and one notes signs of unsteadiness near the trailing edge at  $t = 1.5$ . Thereafter, the boundary layer over the top surface is excited by SBS strip near  $x \simeq 0.25$ . Thus, the frames at  $t = 1.30$  and  $1.50$  correspond to unexcited flow case. When the flow is not excited, disturbances originating from the trailing edge affects flow upstream and the affected region increases with time. This occurs for both upper and lower surface shear layers. This is indicative of upstream propagation of disturbances for this flow, which was also noted for flow past semi-infinite flat plate, with and without heat transfer. The bottom frame in Figure 1f, at  $t = 2.0$  shows effects of SBS excitation which causes downstream propagating disturbances. We note that in developing numerical methods for this and other problems described here, we have taken specific care, with the help of appropriate upwind filters<sup>31</sup>, to avoid spurious upstream propagating numerical disturbances. Thus, the presence of simultaneous upstream and downstream propagating disturbances are physical in nature and capturing these are attributes of high accuracy methods developed for direct simulation.

### III. Characterization of POD Modes

Many earlier studies reported obtaining POD modes appearing pairwise and tried to explain vortex shedding behind bluff bodies by these modes. However, POD mode-pairs and time-varying instability modes have been recently related<sup>8,9</sup> which satisfies an equation originally developed for the amplitude of instability modes ( $A(t)$ ) given by the classical Stuart-Landau (SL) equation<sup>32-34</sup>

$$\frac{d|A|^2}{dt} = 2\sigma_r|A|^2 - l_r|A|^4 \quad (3.1)$$

where  $\sigma_r$  is the exponent of exponential temporal growth rate and  $l_r$  is the Landau coefficient. This equation can be used to study sub-critical instability or super-critical stability depending upon the sign of  $l_r$ . Early applications of POD were used to characterize limit cycle oscillations of dynamical system with single dominant instability mode via nonlinear saturation given by the self-interaction term on the right hand side of Eq. (3.1) for  $l_r > 0$ . This type of modes have been termed as regular  $R_1$ -modes<sup>8,9</sup> corresponding to Strouhal frequency, as well as its higher harmonics (by  $R_2$ -modes). POD analyses in these references, also revealed other modes which do not satisfy Eq. (3.1) and these have been further classified into anomalous modes of first ( $T_1$ ) and second ( $T_2$ ) kinds. Universality of POD modes for vortex-dominated flows have been noted<sup>9</sup>

. In the context of non-regular modes, Noack *et al.*<sup>12</sup> modeled one such mode (called the shift mode), to explain flow evolution past circular cylinder for trans-critical Reynolds numbers. This was developed for the time-averaged flow field and not obtained directly from time-accurate results of full Navier-Stokes equation.

Despite the nonlinearity of Eq. (3.1), this is directly integrable as

$$|A|^2 = \frac{A_0^2}{(A_0/A_e)^2 + [1 - (A_0/A_e)^2] e^{-2\sigma_r t}} \quad (3.2)$$

where  $A_0$  is the value of  $A$  at  $t = 0$ . Here,  $A_e = \sqrt{2\sigma_r/l_r}$  represents the asymptotic value of the solution for  $t \rightarrow \infty$ , for which left hand side of (3.1) is zero. Approach of  $A$  to  $A_e$ , indicates independence of  $A_e$  on  $A_0$  - one reason for which this flow is termed an oscillator. Such a solution is due to particular combination of the  $l_r > 0$  and  $Re > Re_{cr}$  which takes the temporally growing flow to a strictly time periodic neutral state of *supercritical stability*. For supercritical  $Re$ :  $\sigma_r \sim (Re - Re_{cr})$  and thus, a plot of  $A_e$  versus  $Re$  will represent a parabolic variation between the two. It is also expected that Stuart-Landau model has better applicability near  $Re_{cr}$ .

It is important to note for general flows that it is not always possible to describe a steady equilibrium flow whose stability is to be studied. This is specifically true, if one is talking of impulsive start of flow. In Figure 2a, flow past a circular cylinder for  $Re = 100$  and flow inside a square LDC is sampled for  $Re = 8500$  at discrete points. In the frames (i) and (ii), two points are studied - one on the wake center-line at P1 (with  $x = 0.5044$ ,  $y = 0$ ) and another point which is off-center at Q1 (with  $x = 8.0$ ,  $y = 8.0$ ). It is noted that the vorticity value at the center-line reveals a solution which mimics Eq. (3.2). In frame (ii), vorticity variation with time does not follow Eq. (3.2) and it appears to have suffered a *shift* from its early time behavior. Yet it would be improper to term this variation to represent a shift mode. This instead shows a  $R_1$ -mode type variation in conjunction with a secular growth. In both the cases, before the onset of oscillatory growth, original equilibrium condition represents a steady state. In frames (iii) to (vi), vorticity variation with time is depicted for four representative points inside the LDC for  $Re = 8500$ . Both of these flows have started impulsively, which imply that the initial condition for the flow is given by the corresponding inviscid flow past the circular cylinder and a quiescent condition for the flow in square LDC. It is noted that despite such dissimilar initial flows both flows display equivalent disturbance growth histories. In frame (iv), disturbance evolution for point P shows clear regular mode ( $R_1$ ), as in frame (i) for P1. Similarly the oscillatory growth of disturbances at Q and R in frames (v) and (vi) resemble time variation shown for Q1 in frame (ii).

Similarity of the flow fields in Figure 2a can also be viewed with the help of POD characterization through the use of Eq. (1.2) for the disturbance vorticity field obtained from DNS and the POD eigenfunctions

$$a_k(t) = \int \int_S \omega'(\mathbf{X}, t) \phi_k(\mathbf{X}) d^2\mathbf{X} \quad (3.3)$$

Following steps are performed in obtaining POD amplitudes as function of time. Starting from the initial condition, time integration of Navier-Stokes equation using stream function-vorticity provides instantaneous solution for vorticity and velocity fields. Subtracting the equilibrium solution from instantaneous solution, one obtains the disturbance vorticity. With the help of disturbance vorticity in the computational domain, one obtains the correlation matrix,  $[R_{ij}]$  and then using Eq. (1.1), one obtains the eigenvalues,  $\lambda_k$ 's. Using a standard linear algebraic routine, one can obtain the eigenfunctions,  $\phi_k(\mathbf{X})$ 's, converted into an orthonormal basis. Using Eq. (3.3) one obtains the POD amplitudes,  $a_k(t)$ 's.

In performing POD, we have followed the method of snapshots<sup>5,6</sup>. We note that the presented POD analysis here<sup>8,9</sup> is different from that is reported in some other recent works<sup>12,35,36</sup>. In these latter references, analyses is based on spatial singular value decomposition performed on solution of Reynolds average Navier-Stokes equation (RANS) and unsteady RANS solution. Thus, the system portrait obtained by these two ways differ in significant ways. Note that the present approach use the solution of unsteady Navier-Stokes equation without resorting to any models, which is mandatory for RANS and/ or URANS approaches.

Eigenvalues obtained from Eq. (1.1) give the probability of occurrence of various eigenmodes of the disturbance field. Partial sums of the eigenvalues give the cumulative enstrophy of the system,

$$En = \sum_{i=1}^N \omega'(\mathbf{X}_i, t)^2$$

These eigenvalues are dependent on the time interval over which the POD analysis is performed, as has been established in<sup>8</sup> for flow over a single cylinder. Numerical ordering of POD modes indicate the relative

importance of the corresponding modes, i.e., the lower numbered ones contributing larger values. Rationale of numbering these modes are well described<sup>8,9</sup> and is not repeated. In these references, connection between POD and instability modes has been established, which will be restated again. Instability modes which obey SL equation have been termed as  $R_1$ - and  $R_2$ -modes in these references. Additionally, we have also classified POD modes which do not form pairs as instability modes and follow SL equation, in two categories of  $T_1$ - and  $T_2$ -modes. The  $T_1$ -modes resemble shift modes<sup>12</sup>, even though the POD procedures are based on different governing equations. While theoretically it is possible to obtain multiple shift modes,<sup>12,36</sup> investigators using RANS or URANS formulations have reported only single shift mode to explain change in the mean field. In contrast, more than one shift modes have been reported<sup>8,9</sup> using full time dependent Navier-Stokes equation.

In Figure 2b(i), POD amplitude functions are plotted versus time for square LDC problem for  $Re = 8500$ . Plotting of modes in the figure, either individually or in pair are decided by the classification scheme suggested in<sup>8,9</sup>. Here, third and seventh modes do not form pair and such isolated modes are the anomalous  $T_1$ -modes. Corresponding eigenfunctions<sup>9</sup> are characterized by circular vorticity contours in the center, along with corner vortices. The regular modes (first/second and fifth/sixth) are characterized by polygonal vortices, former ones showing triangular core vortex, while the latter ones show hexagonal vortex. Anomalous modes of second kind ( $T_2$ -modes) are noted for this flow field for ninth/tenth and eleventh/twelfth mode pairs characterized by wave-packet like time variation for POD amplitudes. These twelve eigenmodes account for 99.93% of total enstrophy.

In Figure 2b(ii), POD amplitudes are plotted as function of time for flow past circular cylinder for  $Re = 100$ , with numbering sequence as explained earlier.<sup>8</sup> For this case, third and eleventh modes are the  $T_1$ -modes. The first/second modes display  $R_1$ -mode like behavior with time variation given by the periodicity of the Strouhal number. Fifth/sixth mode pair shows variation like regular modes, but the time variation is at higher than Strouhal frequency and hence this is termed as  $R_2$ -mode. Also, amplitude variation shows slight overshoot before settling down to the new equilibrium state. However, time variations shown by seventh/eighth and ninth/tenth modes are not representative of modes satisfying SL equation. Amplitude of  $a_7$  displays wave-packet like variation during disturbance growth phase, while  $a_8$  shows variation like  $R$ -modes. Thus, this pair appears as to be arising due to interaction between  $R$ - and  $T_2$ -modes. Ninth/tenth mode pair displays wave-packet like behavior at early times.

#### IV. Hopf Bifurcation

Hopf bifurcation describes the passage of a dynamical system from an equilibrium state to a periodic state as a typical bifurcation parameter is varied. In this general definition, there are two important aspects. First, through bifurcation the dynamical system transits from one equilibrium state to another. For the case of flow past a circular cylinder the initial equilibrium state is given by a viscous flow, with top-down symmetry. Due to bifurcation, the flow exhibits periodic vortex shedding in the wake. For the case of flow inside LDC, initial equilibrium state is the trivial no-flow condition. Thus, during the bifurcation, the flow exhibits strong transient, as opposed to smooth exponential growth of disturbances for the flow past a cylinder. We have already noted in explaining Eq. (3.2) that the new equilibrium state is independent of initial condition and the amplitude ( $A_e$ ) displays parabolic variation in the neighborhood of  $Re_{cr}$ , provided there is only a single dominant mode, whose nonlinear action is one of self-interaction term, as given by the last term on right hand side of Eq. (3.2). In this scenario, Reynolds number plays the role of deciding parameter for the ensuing bifurcation. To assess the utility of these assumptions in developing SL equation, we have plotted in Figure 3a the variation of  $|A_e|$  with Reynolds numbers. Top frame shows this for square LDC and the variation is not strictly parabolic - implying violation(s) of implicit conditions used in deriving SL equation. This has been shown<sup>8,9</sup> that this is essentially due to the importance of multiple modes and a typical sets of results are given in Figure 3a. Multiple Hopf bifurcation is indicated by locally fitting parabola (as shown by dotted curves) whose intersection with Reynolds number axis indicates different Hopf bifurcation points for square LDC in the top frame and for single circular cylinder in the right frame. In the bottom frame, we have also included the experimental results of Strykowski<sup>37</sup> to show the imprint of multiple Hopf bifurcations of the flow.

In Figure 3b, we have compared the bifurcation diagrams of two side-by-side cylinders with two different gap to diameter ratio of  $s = 3.4$  and  $2.5$ . One noticeable feature of two side-by-side cylinders case with  $s = 3.4$  is the closeness of  $Re_{cr1}$  and  $Re_{cr2}$  with that of the single cylinder case shown in Figure 3a. Presence of the second cylinder moves forward the first Hopf bifurcation, while the second  $Re_{cr}$  is moved to higher Reynolds

number. When the gap between the cylinders is decreased to  $s = 2.5$ , we note that  $Re_{cr1}$  increases again, while the second  $Re_{cr}$  decreases again. Effects of second cylinder in selectively stabilizing and destabilizing the wake of another cylinder are well known<sup>13,38</sup> and the presented bifurcation diagram attests to that.

So far we have discussed Hopf bifurcation with the Reynolds number as the parameter. This can be studied with respect to other parameters as well, as has been performed for the case of a cylinder executing rotary oscillations. The amplitude ( $\tilde{a}$ ) and frequency ( $S_f$ ) of imposed oscillations can be treated as additional parameters, as used here for  $Re = 150$  flow. To study the appearance of dominant frequencies, we have varied  $\tilde{a}$ , while keeping  $S_f = \pi/2$ . In Figure 4a, variation of nondimensional mean drag coefficient is shown with respect to  $\tilde{a}$  and one notices a local minimum at  $\tilde{a} = 0.8$  and a global minimum at  $\tilde{a} = 2.0$ . Here, the drag is non-dimensionalized with respect to the drag value for the unforced case. Hence, all the results shown in Figure 4a represent drag reduction. In addition to this aspect of flow control, one also notes introduction of newer time scales in the flow problem, which is measured here with respect to fluctuating component of drag. The bifurcation diagram is shown with the help of frames in Figure 4b and 4c, with the response amplitude shown in log-scale. In Figure 4b, one notices that at lower amplitudes of excitation, dynamics is determined at the Strouhal frequency ( $f_0 = 0.3711$ ) shown in the frame. It is interesting to note that apart from the presence of this time scale, one also notices multiple additional frequencies. For example, at lower values of  $\tilde{a}$ , one also notices another detuned peak at  $f_1 = 0.3320$  and a very low frequency event which is at the detuning value of  $f_2 = 0.0391$ . There are also other detuned frequencies, which are noted in Figure 4c, in addition to other peaks at higher superharmonics and their detuned values - all of which decay in importance with increase in the value of  $\tilde{a}$ , except a single one at  $f = 3f_1 - 2f_2 = 0.9961$ . This dominant frequency component is displayed in Figure 4b.

Displayed mean drag variation in Figure 4a shows the local and global minima for  $\tilde{a} = 0.8$  and 2, respectively. In Figure 5a, the POD amplitudes and their FFT's are shown for  $\tilde{a} = 0.8$  in the top frames, while the bottom two frames show the time variation of lift and drag for this case. We note that the first and the fourth modes are directly due to the forcing and the amplitude is non-zero, right from the onset. Whereas, second/third modes form almost a regular  $R_1$ -mode. All the other displayed mode pairs show  $T_2$ -mode variations. Time variations shown by seventh/eighth and ninth/tenth mode pairs show typical behavior not seen in unforced dynamics. Such time variation is also reflected in the time variation of lift and drag, shown at the bottom.

Dynamics of this flow case is also understood better by looking at the corresponding eigenfunctions and their contributions to the enstrophy distribution as shown in Figure 5b. First and fourth modes show similar eigenfunctions, although the first mode contributes more than three times that of the fourth mode. Second/third mode also contributes little more than one third of the total enstrophy. Interestingly, the higher modes do not represent a significant contribution, when viewed over the full time range, yet these affect periodic spurt in contribution, as evidenced from total load variation in the bottom two frames.

In Figure 5c, the eigenfunctions are shown for the case where maximum drag reduction is obtained. Here, it is noted that the first two modes account for more than ninety percent of total enstrophy, while the other higher modes have little contributions. More importantly, the first two modes also display two trains of vortices ejected from the shoulders, which are symmetric and create a jet-like flow in the near wake. This is to be contrasted with the Karman vortex sheet, which is shed alternately from either side.

So far we have discussed about bifurcations, where the onset is often associated with temporal instability that is defined by linear dynamics and gradual exponential growth. In Figure 6, we show the time variation of the POD amplitudes for the case of two side-by-side cylinders for  $Re = 100$  and  $s = 2.5$ . These two cylinders are identified as  $Cy_0$  and  $Cy_1$  and displayed four modes account for more than ninety five percent of total enstrophy. This flow also shows either in-phase or out-of-phase amplitude variation for the two cylinders in the displayed modes. The first mode displays the curious behavior of sudden in-phase oscillation beginning at  $t \simeq 120$  and this phenomenon has been termed as *flip-flopping* in the literature. From the perspective of POD and instability modes, this phenomenon actually fixes the new equilibrium state. Thus in this case, arrival at the new equilibrium state is almost instantaneous and not gradual, as was noted for square LDC and single cylinder cases. Second and third POD modes display anti-phase oscillation after the new equilibrium state is reached. These two form a pair and constitute a  $R$ -mode. The first mode clearly shows that the two cylinders move in phase - a simultaneous heaving motion caused by the presence of one cylinder with the second. For higher gap ratios, first mode is no more seen. While the first three modes show single dominant frequency oscillations, the fourth mode shows presence of multiple dominant modes. The *flip-flopping* phenomenon has been displayed in the time variation of drag for both the cylinders shown

in the bottom frame.

Above examples show the importance and appearance of higher modes due to nonlinear dynamics. We also note that rotary oscillation for the circular cylinder causes bypass transition events and is associated with vortex dominated flows. In the following, case of flow past semi-infinite flat plate is discussed which shows bypass events even when the amplitude of excitation is very low. This is also relevant now to relate POD modes with instability modes, as some of the POD modes for vortex dominated flows displayed time variation, which has been shown by instability modes following SL equation.

## V. Relating POD and Instability Modes

In contrast to vortex dominated flows, few studies reported using POD to study instability of flow past streamlined bodies. Rempfer and Fasel<sup>39, 40</sup> have attempted to relate regular POD modes with coherent structures in the flow. The  $j^{th}$  coherent structure have been defined as a sum of  $2j^{th}$  and  $(2j - 1)^{th}$  pair-forming POD modes in these references as

$$\rho_j(\vec{X}, t) = a_{2j}(t) \phi_{2j}(\vec{X}) + a_{2j-1}(t) \phi_{2j-1}(\vec{X}) \quad (5.1)$$

Note that this splitting does not require that the pairs to be orthogonal to each other. A consistent splitting is given in Eqs. (5.1) and (5.2) of Sengupta *et al.*<sup>8</sup>. For example, unstable flow's vorticity perturbation can be expressed by Galerkin-type expansion in terms of various instability modes<sup>34</sup>

$$\omega'(\vec{X}, t) = \sum_{j=1}^{\infty} [A_j(t) f_j(\vec{X}) + A_j^*(t) f_j^*(\vec{X})] \quad (5.2)$$

where quantities with asterisks again denoting complex conjugates. Here, corresponding to  $j^{th}$  instability mode,  $A_j(t)$  denotes time-dependent amplitude and  $f_j(\vec{X})$  describes space-dependent eigenfunction that satisfies prescribed boundary conditions. The instability modes are related to POD modes by defining a normalization factor  $\epsilon_j = (\lambda_{2j} + \lambda_{2j-1}) / \sum_{k=1}^N \lambda_k$ . By noting that pair-forming POD modes have a phase shift of  $90^\circ$  (which is true in a time averaged sense except during the transient stage, as shown below),  $A_j(t)$  and  $f_j(\vec{X})$  can be defined in terms of the POD modes as

$$A_j(t) = \sqrt{\epsilon_j} [a_{2j-1}(t) + i a_{2j}(t)] \quad (5.3)$$

$$f_j(\vec{X}) = \frac{1}{2\sqrt{\epsilon_j}} [\phi_{2j-1}(\vec{X}) - i \phi_{2j}(\vec{X})] \quad (5.4)$$

Implicit in the above definition of instability modes is the assumption that pair-forming POD modes have a phase difference  $\Delta\theta = 90^\circ$ . This aspect is re-investigated for flow past a semi-infinite flat plate, with and without heat transfer. In the top frame of Figure 7, the computational domain used to study nonlinear receptivity over the semi-infinite flat plate is shown - excited by the SBS strip. In the general case shown in the sketch, edge of velocity and thermal boundary layers are identified and for the heat transfer case, apart from the vortical excitation applied at the wall, a very specific wall temperature distribution is prescribed to achieve the similarity profile obtained by Schneider<sup>30</sup>. This involves zero heat transfer from the plate everywhere, except at the leading edge of the plate, where all the heat transfer takes place, so that the wall temperature is given by,  $T_w(x) \sim x^{-1/2}$ . Vorticity contour plots are compared for the cases of without heat transfer (on the left panels) and with heat transfer (on the right panels) in Figure 7. Two aspects are notable from this figure on flow receptivity. First, vortical wall excitation gives rise to response field, which creates a local solution, apart from the almost stationary TS wave-packet and a leading spatio-temporal wave front. The latter causes unsteady separation on the wall in both the cases, which also causes massive wall-normal eruptions piercing through the wall boundary layer. Second, a lower frequency excitation ( $F = 4.5 \times 10^{-5}$ ) for the case with heat transfer and amplitude control parameter in Eqs. (2.1) to (2.3) kept at a lower value of  $\alpha_1 = 0.002$  causes a larger instability as compared to the case of flow without heat transfer, for  $F = 10^{-4}$  and  $\alpha_1 = 0.01$ . Sequences of flow evolution is typical of bypass transition recorded for sub-critical transition<sup>41, 42</sup> caused by aperiodic vortex translating in the free stream. Vortical eruptions associated with spatio-temporal wave front for both the cases, implies that this plays a larger role in the transition process, quite contrary to the commonly held belief that TS waves cause flow transition.

In Figure 8, POD amplitudes are shown for the case of no heat transfer, for a data set up to  $t = 60$ , with a very fine time interval of  $\Delta t = 0.01$ , to enable one to include very high frequencies. The plots are shown by pairing appropriate modes, as shown, e.g., by pairing first/second, fifth/sixth, ninth/tenth, eleventh/twelfth modes. From these plots, using the convention set up earlier<sup>8,9</sup>, we note that first/second pair forms  $R_1$ -mode. In contrast, ninth/tenth modes fluctuate at twice the frequency of first/second pair and hence, this is termed as  $R_2$ -mode. Third, seventh and thirteenth POD modes are the isolated  $T_1$ -modes. Fifth/sixth and eleventh/twelfth pairs form  $T_2$ -modes. In addition to these modes, one also notices fifteenth/sixteenth and seventeenth/eighteenth pairs, which cannot be classified as  $T_2$ -mode, although these appear as packets. The correspondence of these modes with spatio-temporal front is also noted in the concurrency of the two in the time-plane. Although it is not shown here, the spatio-temporal fronts eventually lead to flow transition and is central to understanding the interrelationship between instability and transition.

In Figure 9, POD eigenfunctions are shown plotted and one can clearly discern the pairing process further. Also, the  $T_1$ -modes have a typical eigenfunction that is noted for the third mode. Its presence is noted by pair of elongated vortices formed over the plate, which cause the mean field to shift. For this mode, vortices of alternate signs are seen to stack one on top of each other. The  $T_2$ -mode as shown here for eleventh/twelfth mode pair shows the spatial distribution, which also resembles multiple wave-packets. The new POD modes revealed here for the spatio-temporal front, also display atypical eigenfunctions.

So far, we have stated that the mode pairs are plotted together, as these are phase shifted by  $\Delta\theta = \pi/2$  and this led to the definition provided in Eqs. (5.3) and (5.4). This assumption of the phase shift can be tested strictly, in terms of an arbitrary phase shift as well. The definition of the time-dependent amplitude  $A_j(t)$  and the space-dependent variation  $f_j(\vec{X})$  of the instability mode can be modified by incorporating exact phase difference  $\Delta\theta$  between the pair forming POD modes by

$$A_j(t) = \sqrt{\epsilon_j}[a_{2j-1}(t) + e^{i\Delta\theta} a_{2j}(t)] \quad (5.5)$$

$$f_j(\vec{X}) = \frac{1}{2\sqrt{\epsilon_j}}[\phi_{2j-1}(\vec{X}) - e^{i\Delta\theta} \phi_{2j}(\vec{X})] \quad (5.6)$$

In Figure 10, phase difference  $\Delta\theta$  between four different pairs have been plotted as a function of time. It is seen that the phase difference between the first and the second modes is not  $90^\circ$ , initially. It starts from a lower value of  $50^\circ$  and finally the mean settles down to  $90^\circ$ , with high frequency fluctuations about it. Similar features are noted for eleventh/twelfth pair, for which  $\Delta\theta$  initially starts from a lower value and the mean settles down to a value around  $90^\circ$ . One however notices in Figure 10, occurrence of larger fluctuations for  $\Delta\theta$  at around  $t = 42$  for this pair. This causes a deviation in  $\Delta\theta$  of about  $\pm 10^\circ$  about the mean value  $\Delta\theta_m \simeq 90^\circ$ . It has been observed that at around this time, corresponding amplitudes take a low value. The mean phase difference  $\Delta\theta_m \simeq 90^\circ$  for fifth/sixth and ninth/tenth modes are noted from the beginning with approximate fluctuations of  $\Delta\theta$  of  $\pm 3^\circ$  for the fifth/sixth modes and of  $\pm 6^\circ$  for the ninth/tenth modes.

Correct phase shifted instability mode pairs given by Eqs. (5.5) and (5.6) are formed in the present exercise and are shown in Figure 11. It is clearly noted that only a very few modes show time variation which can be identified with that given by SL equation. Even, the first and fifth instability modes have earlier transients which are different from that is noted for flow past single circular cylinder, for trans-critical Reynolds numbers. Corresponding modulus of space dependent functions for the instability modes are shown in Figure 12. The isolated modes (second, fourth and seventh instability modes) are associated with  $T_1$ -modes. The first and the fifth instability modes are associated with regular POD modes, while the third and the sixth instability modes are associated with  $T_2$  modes. The eighth and the ninth instability modes are associated with the spatio-temporal wave fronts.

It is important to note the constituents of some of the special POD modes observed. For example, eleventh/twelfth modes display very atypical wave-packet like time variation, as shown in the top frame of Figure 13. Fourier transform of the time series displays the global maximum for  $\beta \Delta t = 0.07234$  and wave-packet like behavior is due to sideband interactions with the peak. Note that this is also the peak that is responsible for the first/second  $R$ -mode, fifth/sixth  $T_2$ -mode. In the frames (ii) to (vii) of Figure 13, we have progressively used wider bands of frequencies (indicated by  $\Delta\beta\Delta t$ ) to reproduce the actual signal for  $a_{11}(t)$ . It is noted that one requires at least  $\pm 10.2\%$  of the sideband around the peak to have a meaningful reproduction of the original signal. Same observation also holds for  $a_{12}(t)$ ,  $a_5(t)$  and  $a_6(t)$ . This reproduced signal has minor mismatches for  $t \rightarrow 0$  and  $\infty$ , due to Abel's and Tauber's theorem<sup>28</sup>.

Flow past SHM-1 aerofoil at a cruise Reynolds number of  $10.3 \times 10^6$  is more complex as compared to flow past a flat plate. For the aerofoil case, pressure gradient continuously varies over the aerofoil surface, causing

it to make the flow more receptive to background disturbances in regions of adverse pressure gradient and where unsteady effects are predominant, as in the case of flow near the trailing edge, on the lower surface. We have first computed flow around SHM-1 aerofoil at  $Re = 10.3 \times 10^6$  and zero degree angle of attack (AOA) for the unexcited case using  $(597 \times 397)$  grid. We have used 800 snapshots for a data set from  $t = 0.025$  to 20 for the POD analysis and corresponding eigenfunctions are shown in Figure 14a. Importance of a particular mode is shown by the amount of enstrophy carried by individual modes. As shown in the figure, first and seventh modes are anomalous  $T_1$ -modes. First mode carries 22.07% of total enstrophy and shows formation of shear layer kind of flow structures on the aerofoil surface. Pair formed by third and fourth mode shows longer, elongated flow structures, as compared to pair formed by fifth/sixth mode and by ninth/tenth mode. Figure 14b shows POD amplitude functions in the right column. Variations of these POD amplitude functions with time show presence of multiple frequencies and corresponding FFT's are plotted in the left column. From the FFT plots one can observe presence of dominant  $N_1$  frequency in all of the shown modes except the seventh mode. Modulus of instability mode amplitude functions are shown in Figure 14c. Similar to POD amplitude function plots in Figure 14c, one can observe higher instability modes containing larger band of frequencies.

We have studied flow past a SHM-1 aerofoil when the wall-excitation is applied for the cruise Reynolds number. For this case, we have used a fine grid with  $(5169 \times 577)$  grid points. First, we have computed flow field up to  $t = 1.5$  without excitation. Variation of vorticity with time at three different points on the aerofoil top surface is shown in Figure 15a(i). Large fluctuations present in surface vorticity during initial phase of flow development become negligible around  $t = 1.5$  as shown in the plot. We have shown variation of displacement thickness ( $\delta^*$ ) and nondimensional pressure gradient parameter  $m = \frac{x}{U_e} \frac{\partial U_e}{\partial x}$  on the top surface of the aerofoil at  $t = 1.50$  in frames (ii) and (iii), respectively.  $U_e$  is the edge velocity of the shear layer. A horizontal dashed line corresponding to  $m = -0.09$  shown in the plot corresponds to steady flow separation criteria. This value of pressure gradient is present close to mid-chord location on the top surface of the aerofoil. We have chosen an exciter location of  $x = 0.25$  on the top surface. At this exciter location value of  $m$  is 0.0161, which shows a favorable pressure gradient region and Reynolds number based on the displacement thickness is 2246.8. This is shown by a vertical dashed line in frame (iv) of Figure 15a. For the SBS excitation, we have chosen a frequency of  $F = 1.11441 \times 10^{-5}$  with a amplitude of 0.001. This frequency is marked in the neutral curve as shown in frame (iv). In Figure 15b, frames (i) to (iv) show variation of azimuthal component of the velocity ( $u$ ) on the top surface of the aerofoil at a distance of  $1.242 \times 10^{-6}$  from the surface. We have started the wall-excitation from  $t = 1.50$  onwards. At  $t = 1.50$ , one observes formation of wavy disturbances from  $x = 0.50$  onwards. Presence of adverse pressure gradient towards trailing edge of the aerofoil causes formation of larger amplitude disturbances as shown in the figure. In the subsequent time frames, one observes formation of a wavefront which travels towards the trailing edge of the aerofoil causing further disturbances. Location of the exciter is marked with vertical arrows in these frames. We have performed the POD analysis with 401 snapshots from time  $t = 1.50$  to 5.50. Cumulative enstrophy content is shown in frame (v) of Figure 15b. The first mode only contributes 0.0272 of the total enstrophy which is almost ten times smaller as compared to the unexcited case discussed in Figure 14a. We have shown cumulative enstrophy distribution for first 110 modes in Figure 15b which corresponds to 0.8075 of total enstrophy. This plot suggest that for the excitation case, one needs larger number of modes to reconstruct flow correctly. Eigenfunction variation for this case, on the top surface at a distance of  $1.2465 \times 10^{-5}$  from the surface of the aerofoil is shown in Figure 15c for first nine modes. First two modes form a pair with their individual enstrophy content of 0.0272 and 0.0258, as marked in the figure. Modes three, five, seven and nine do not form a pair. Variation of POD amplitude function with time in Figure 15d shows presence of large band of frequencies as evident from the FFT plots shown in the left column. Even though POD amplitude function shows presence of large band of frequencies, dominant frequencies  $M_1$ ,  $M_2$  and  $M_3$  are present in most of the amplitude functions.

## VI. POD analysis of Complex Flows

In Figure 8, we have noted that spatio-temporal fronts create a new type of POD modes, as shown in frames (viii) and (ix) for fifteenth/sixteenth and seventeenth/eighteenth modes. Despite the low amplitude and lower contribution to total enstrophy (less than even half a percent of the total), these modes play the most significant role in destabilizing the flow by directly being responsible for the ensuing bypass transition. However, this is also the essence of all instabilities which originate by imperceptible causes to produce large

irreversible effects. Presented results here for various flows should be viewed as cautionary in performing reduced order modeling, for unstable and transitional flows, where one must perform time accurate simulations and track as many modes as possible. Eventually a mode's contribution will be determined by the receptivity of the flow to that class of modes.

As an example, we show in Figure 16 the POD amplitude variation for disturbance temperature field created by vortical excitation by SBS strip, with time for the case of flow past a heated semi-infinite flat plate. Results for disturbance velocity have already been shown in frames (i) and (ii) of Figure 1e. Displayed six modes in Figure 16 account for 99.92% percent of a measure defining disturbance temperature field, with the first mode itself accounting for 98.11% of the total. It is interesting to note that the third and fourth modes constitute regular  $R_1$ -modes and the fifth/sixth modes are due to the spatio-temporal front for the disturbance temperature which actually account for trace amount to a measure for the disturbance temperature field. As noted above, eventual flow transition is dictated upon by these fifth/sixth modes. Third/fourth modes represent a single dominant frequency along with sidebands which causes a very well defined modulation of these modes.

Finally, we show the leading eigenfunctions for the case of rectangular LDC (with depth to width ratio of 2:1) in Figure 17, for which instantaneous snapshot of vorticity distribution is shown for  $Re = 6000$  at  $t = 600$  in Figure 1b. Displayed eigenfunction in Figure 17 have been computed for the new equilibrium state and data has been taken from  $t = 1287$  to 1487. In the bottom of each frames, cumulative enstrophy is indicated and one notes these to account for 99.65% of total enstrophy. This case is interesting as it shows Kelvin-Helmholtz instability for the lower cell in the cavity, which is captured in Figure 1b. This is in addition to the polygonal vortical structure noted in the top half of the cavity by viscous temporal instability. Eigenfunctions in Figure 17 show multi-cellular structures for all the modes, with number of cells increasing with mode numbers, by four for the successive mode pairs. These are all  $R$ -modes.

## VII. Conclusion

Here, POD has been used in further explaining the topology and structures of prototypical instabilities of some generic flow fields. This is an extension of classifying POD modes as universal modes shown between an internal and an external flows<sup>8,9</sup>. We have added cases of forced excitation problems and problems which are not seemingly vortex-dominated flows (as in the case of semi-infinite flat plate, with and without heat transfer) and these latter have helped us find a new mode type associated with spatio-temporal growing fronts - shown for flow past a flat plate and also flow past a NLF aerofoil.

We have also investigated flow fields which are geometrically more complex - for example the flow past two side-by-side cylinders and flow inside a rectangular cavity which show more complex flow instability patterns while the POD modes have the basic modes already identified. Present approach helps us undertake nonlinear receptivity studies without making simplifying assumptions, as is usually the case for linear stability approaches. However, the most important issue of tracking intermittent turbulent state of flow, starting from the receptivity stage is achieved finally.

## References

- <sup>1</sup>Kosambi, D. D., "Statistics in Function Space," *J. Indian Math. Soc.*, Vol. 7, 1943, pp. 76–88.
- <sup>2</sup>George, W. K., "Some Thoughts on Similarity, the POD, and Finite Boundaries," *Fundamental Problematic Issues in Turbulence*, Birkhauser Verlag., 1999.
- <sup>3</sup>Lumley, J. L., "The Structure of Inhomogenous Turbulence," *Atmospheric Turbulence and Wave Propagation.*, 1967, pp. 166–178.
- <sup>4</sup>Holmes, P., Lumley, J. L., and Berkooz, G., *Turbulence, Coherent Structures, Dynamical Systems and Symmetry*, Cambridge Univ. Press., 1996.
- <sup>5</sup>Sirovich, L., "Turbulence and Dynamics of Coherent Structures, Part I- III," *Quarterly of Applied Mathematics*, Vol. 45, 1987, pp. 561–590.
- <sup>6</sup>Sirovich, L., "Analysis of Turbulent Flows by Means of the Empirical Eigenfunctions," *Fluid Dynamics Research*, Vol. 8, 1991, pp. 85–100.
- <sup>7</sup>Couplet, M., Basdevant, C., and Sagaut, P., "Calibrated Reduced-Order POD-Galerkin System for Fluid Flow Modelling," *J. Comp. Phys.*, Vol. 207, 2005, pp. 192–220.
- <sup>8</sup>Sengupta, T. K., Singh, N., and Suman, V. K., "Dynamical System Approach to Instability of Flow Past a Circular Cylinder," *Journal of Fluid Mechanics*, Vol. 656, 2010, pp. 82–115.
- <sup>9</sup>Sengupta, T. K., Vijay, V. V. S. N., and Singh, N., "Universal instability modes in internal and external flows," *Computers and Fluids*, Vol. 40, 2011.
- <sup>10</sup>Deane, A. E., Kevrekidis, I. G., Karniadakis, G. E., and Orszag, S. A., "Low-Dimensional Models for Complex Geometry Flows: Application to Grooved Channels and Circular Cylinders," *Phys. Fluids A*, Vol. 3, 1991, pp. 2337–2354.
- <sup>11</sup>Ma, X. and Karniadakis, G. E., "A Low Dimensional Model for Simulating Three-Dimensional Cylinder Flow," *J. Fluid Mech.*, Vol. 458, 2002, pp. 181–190.
- <sup>12</sup>Noack, B. R., Afanasiev, K., Morzynski, M., Tadmor, G., and Thiele, F., "A Hierarchy of Low-Dimensional Models for the Transient and Post-Transient Cylinder Wake," *J. Fluid Mech.*, Vol. 497, 2003, pp. 335–363.
- <sup>13</sup>Dipankar, A., Sengupta, T. K., and Talla, S. B., "Suppression of Vortex Shedding Behind a Circular Cylinder by Another Control Cylinder at Low Reynolds Numbers," *J. Fluid Mech.*, Vol. 573, 2007, pp. 171–190.
- <sup>14</sup>Sengupta, T. K., Suman, V. K., and Singh, N., "Solving Navier-Stokes equation for flow past cylinders using single-block structured and overset grids," *Journal of Computational Physics*, Vol. 229, 2010.
- <sup>15</sup>Bhumkar, Y. G. and Sengupta, T. K., "Drag reduction by rotary oscillation for flow past a circular cylinder," *International Journal of Emerging Multidisciplinary Fluid Sciences*, Vol. 1, No. 4, 2009, pp. 269–298.
- <sup>16</sup>Sengupta, T. K., Lakshmanan, V., and Vijay, V. V. S. N., "A new combined stable and dispersion relation preserving compact scheme for non-periodic problems," *Journal of computational Physics*, Vol. 228, 2009, pp. 3048–3071.
- <sup>17</sup>Sengupta, T. K., Vijay, V. V. S. N., and Bhaumik, S., "Further improvement and analysis of CCD scheme: Dissipation discretization and de-aliasing properties," *Journal of Computational Physics*, Vol. 228, 2009, pp. 6150–6168.
- <sup>18</sup>Bruneau, C. and Jouron, C., "An efficient scheme for solving the incompressible Navier-Stokes equations," *J. Comput. Phys.*, Vol. 89, No. 2, 1990, pp. 389–413.
- <sup>19</sup>Fasel, H. and Konzelmann, U., "Non-Parallel Stability of a Flat-Plate Boundary Layer Using the Complete Navier-Stokes Equations," *J. Fluid Mech.*, Vol. 221, 1990, pp. 311–347.
- <sup>20</sup>Sengupta, T. K., Bhaumik, S., Singh, V., and Shukla, S., "Nonlinear and Nonparallel Receptivity of Zero-Pressure Gradient Boundary Layer," *International Journal of Emerging Multidisciplinary Fluid Sciences*, Vol. 1, No. 1, 2009, pp. 19–35.
- <sup>21</sup>Sengupta, T. K., "Impulse response of laminar boundary layer and receptivity," 1991.
- <sup>22</sup>Sengupta, T. K., Ballav, M., and Nijhawan, S., "Generation of Tollmien-Schlichting waves by harmonic excitation," *Phys. Fluids*, Vol. 6, 1994, pp. 1213–1222.
- <sup>23</sup>Tollmien, W., "The production of turbulence," *NACA TM - 609*, 1931.
- <sup>24</sup>Schlichting, H., "Zur ensteheung der turbulenz bei der plattenströmung," *Nachr. Ges. Wiss. Göttingen, Maths-Phys.*, 1933.
- <sup>25</sup>G. B. Schubauer & Skramstad, H. K., "Laminar boundary layer oscillations and the stability of laminar flow," *J. Aero. Sci.*, Vol. 14, 1947.
- <sup>26</sup>Sengupta, T. K., Rao, A. K., and Venkatasubbaiah, K., "Spatiotemporal Growing Wave Fronts in Spatially Stable Boundary Layer," *Physical Review Letters*, Vol. 96, 2006, pp. 224504.
- <sup>27</sup>Sengupta, T. K., Rao, A. K., and Venkatasubbaiah, K., "Spatio-Temporal Growth of Disturbances in a Boundary Layer and Energy Based Receptivity Analysis," *Physics of Fluids*, Vol. 18, 2006, pp. 094101.
- <sup>28</sup>Sengupta, T. K. and Poinsot, T., *Instabilities of Flows: with and without Heat Transfer and Chemical Reaction*, Springer Wien New York, 2010.
- <sup>29</sup>Unnikrishnan, S., *Linear stability analysis and nonlinear receptivity study of mixed convection boundary layer developing over a heated flat plate*, M. Tech. Thesis, I. I. T. Kanpur, 2011.
- <sup>30</sup>Schneider, W., "A similarity solution for combined forced and free convection flow over a horizontal plate," *Int. J. Heat Mass Transfer*, Vol. 22, 1979, pp. 1401–1406.
- <sup>31</sup>Sengupta, T. K., Bhumkar, Y. G., and Lakshmanan, V., "Design and analysis of a new filter for LES and DES," *Computers and Structures*, Vol. 87, 2009, pp. 735–750.
- <sup>32</sup>Landau, L. D., "On the Problem of Turbulence," *C. R. Acad. Sci. USSR*, Vol. 44, 1944, pp. 311–315.
- <sup>33</sup>Stuart, J. T., "On the Non-Linear Mechanics of Wave Disturbances in Stable and Unstable Parallel Flows. Part 1. The Basic Behaviour in Plane Poiseuille Flow," *Journal of Fluid Mechanics*, Vol. 9, 1960, pp. 353–370.
- <sup>34</sup>Drazin, P. G. and Reid, W. H., *Hydrodynamic Instabilities*, Cambridge Univ. Press., 1981.

<sup>35</sup>Luchtenburg, D. M., Guenther, B., Noack, B. R., King, R., and Tadmor, G., "A Generalized Mean-Field Model of the Natural and High-Frequency Actuated Flow around a High-Lift Configuration," *J. Fluid Mech.*, Vol. 623, 2009, pp. 283–316.

<sup>36</sup>Siegel, S. G., Seidel, J., Fagley, C., Luchtenburg, D. M., Cohen, K., and McLaughlin, T., "Low-Dimensional Modelling of a Transient Cylinder Wake Using Double Proper Orthogonal Decomposition," *Journal of Fluid Mechanics*, Vol. 610, 2008, pp. 1–42.

<sup>37</sup>Strykowski, P. J., *The control of absolutely and convectively unstable shear flows*, PhD thesis, Yale University, 1986.

<sup>38</sup>Strykowski, P. J. and Sreenivasan, K. R., "On the formation and suppression of vortex shedding at low Reynolds number," *Journal of Fluid Mechanics*, Vol. 218, 1990, pp. 74–107.

<sup>39</sup>Rempfer, D. and Fasel, H. F., "Evolution of Three-Dimensional Coherent Structures in a Flat-Plate Boundary Layer," *Journal of Fluid Mechanics*, Vol. 260, 1994, pp. 351–375.

<sup>40</sup>Rempfer, D. and Fasel, H. F., "Dynamics of Three-Dimensional Coherent Structures in a Flat-Plate Boundary Layer," *Journal of Fluid Mechanics*, Vol. 275, 1994, pp. 257–283.

<sup>41</sup>Sengupta, T. K., De, S., and Sarkar, S., "Vortex-Induced Instability of an Incompressible Wall-Bounded Shear Layer," *Journal of Fluid Mechanics*, Vol. 493, 2003, pp. 277–286.

<sup>42</sup>Lim, T. T., Sengupta, T. K., and Chattopadhyay, M., "A Visual Study of Vortex-Induced Subcritical Instability on a Flat Plate Laminar Boundary Layer," *Expts. Fluids*, Vol. 37, 2004, pp. 47–55.

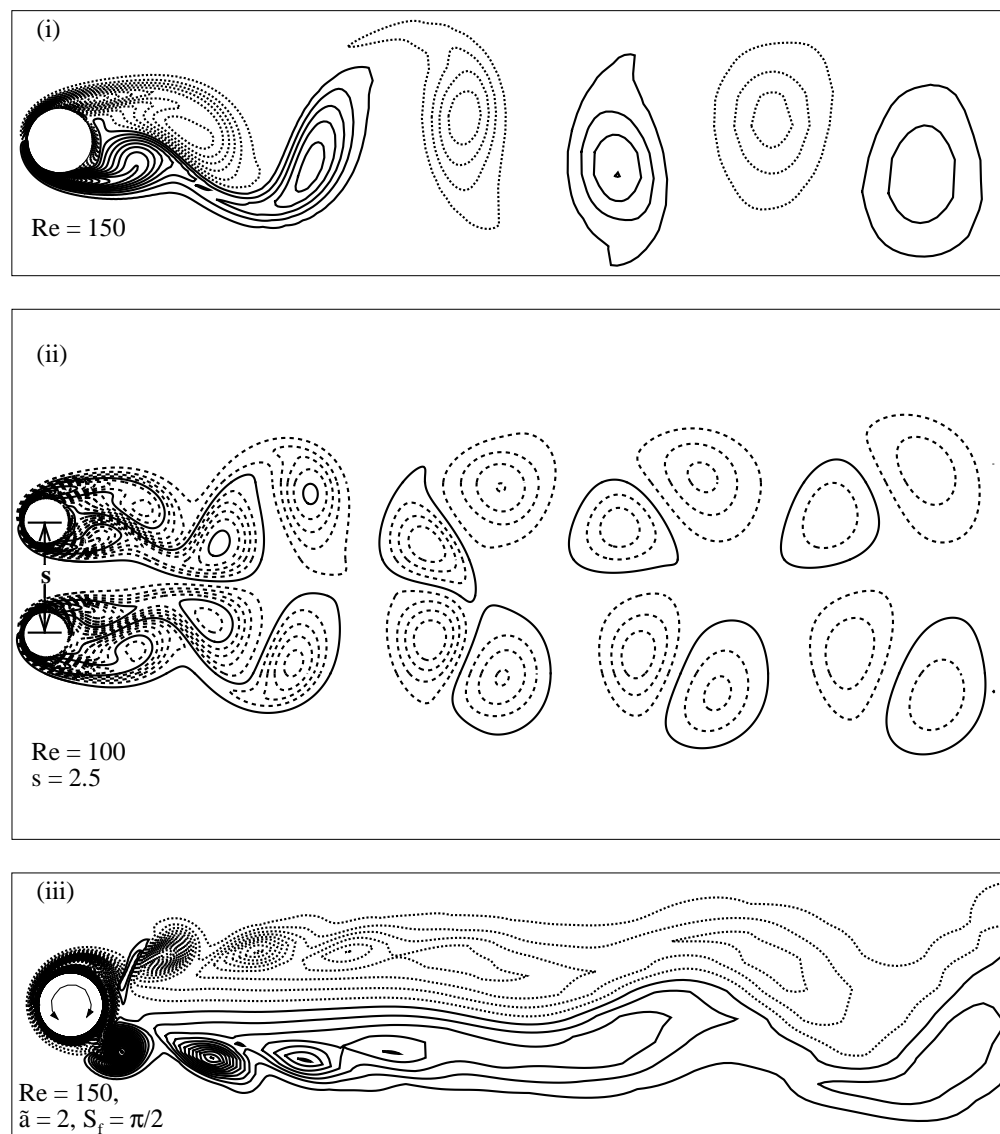


Figure 1a Typical vorticity contours for (i) flow past a cylinder for  $Re = 150$ ; (ii) flow past two side-by-side stationary cylinders, separated by a gap of  $s^* = 2.5d^*$ , for  $Re = 100$  (iii) flow past a circular cylinder performing rotary oscillation for  $Re = 150$ ,  $\tilde{\alpha} = 2$ ,  $S_f = \pi/2$ .

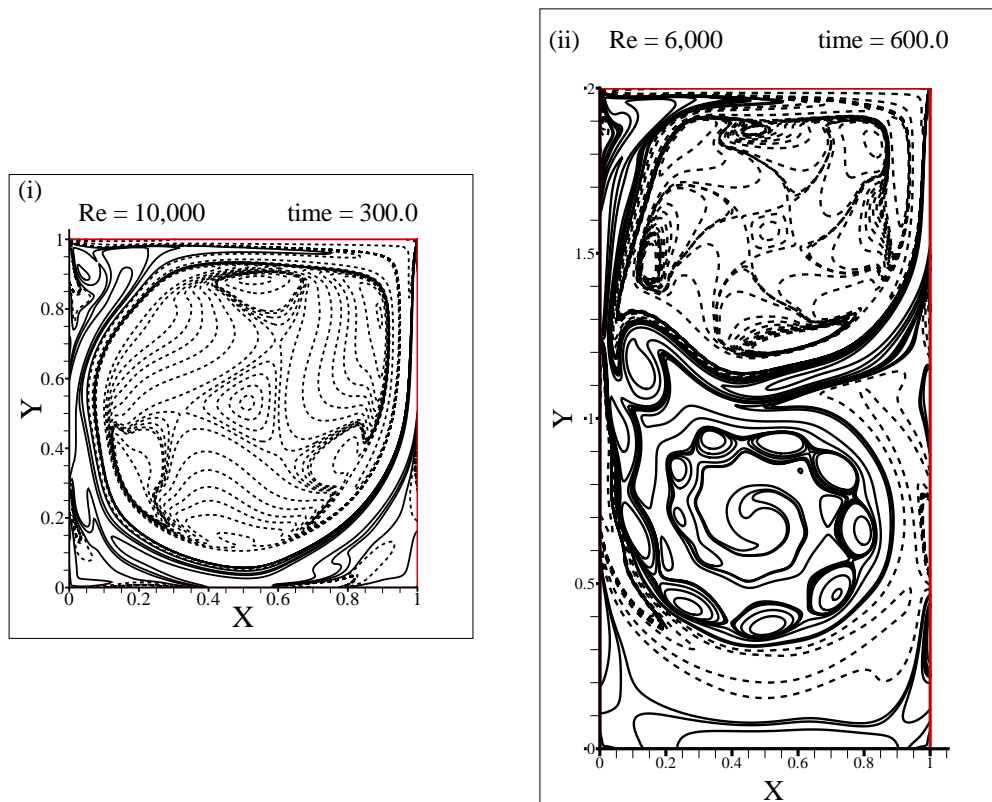


Figure 1b Typical vorticity contours for flow inside a (i) square lid driven cavity for  $Re = 10000$  and (ii) rectangular lid driven cavity (2 : 1 aspect ratio) for  $Re = 6000$ .

(i) Schematic diagram of the problem

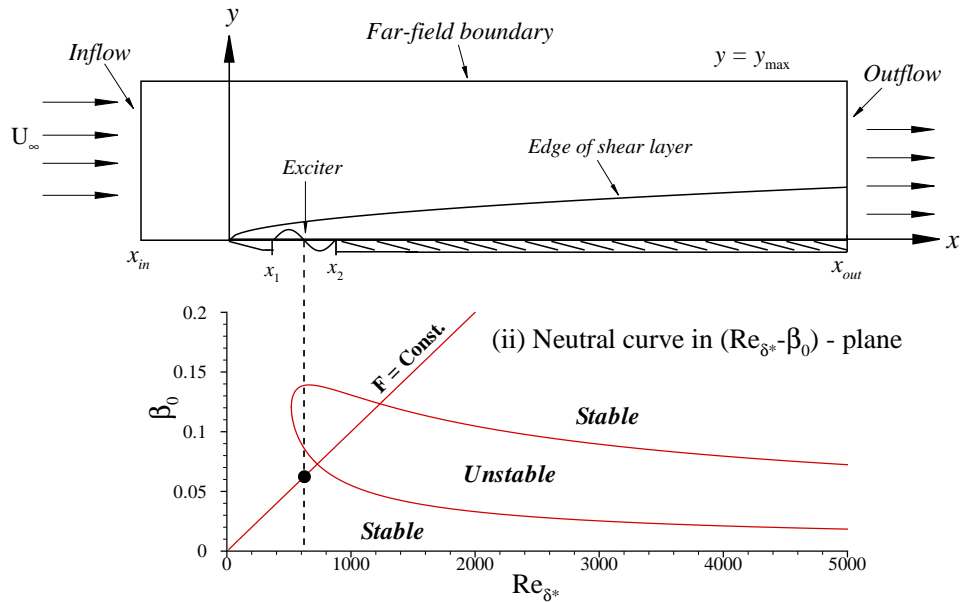


Figure 1c (i) Schematic of the flow and the computational domain including the simultaneous blowing and suction (SBS) strip and (ii) the neutral curve based on linear stability theory

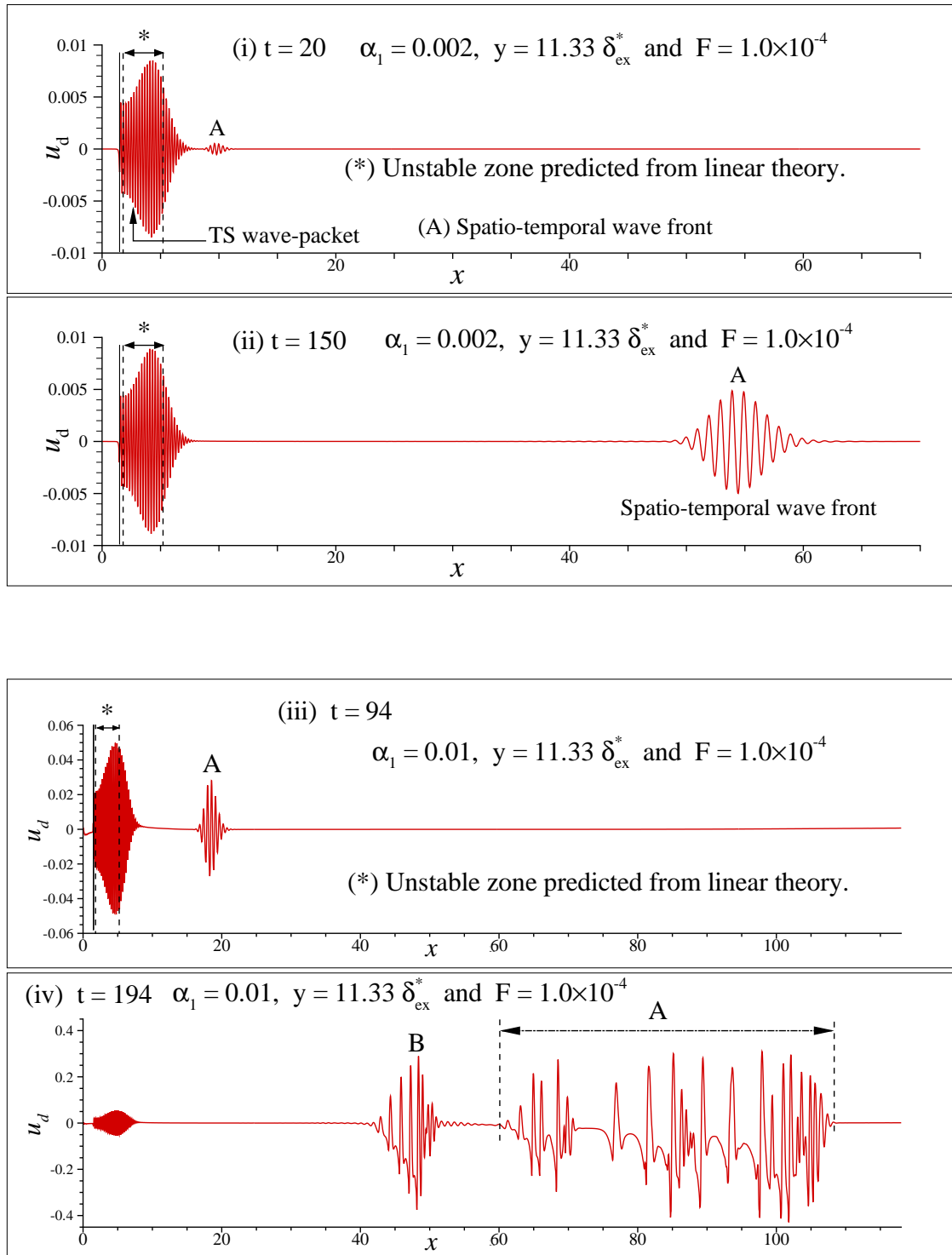


Figure 1d Disturbance streamwise velocity  $u_d$  plotted at indicated times after the onset of excitation, plotted for  $y = 11.33\delta_{ex}^*$  for indicated amplitudes and frequencies of excitation, for flow past a semi-infinite isothermal horizontal flat plate without heat transfer. Here,  $\delta_{ex}^*$  indicates the displacement thickness at the exciter location.

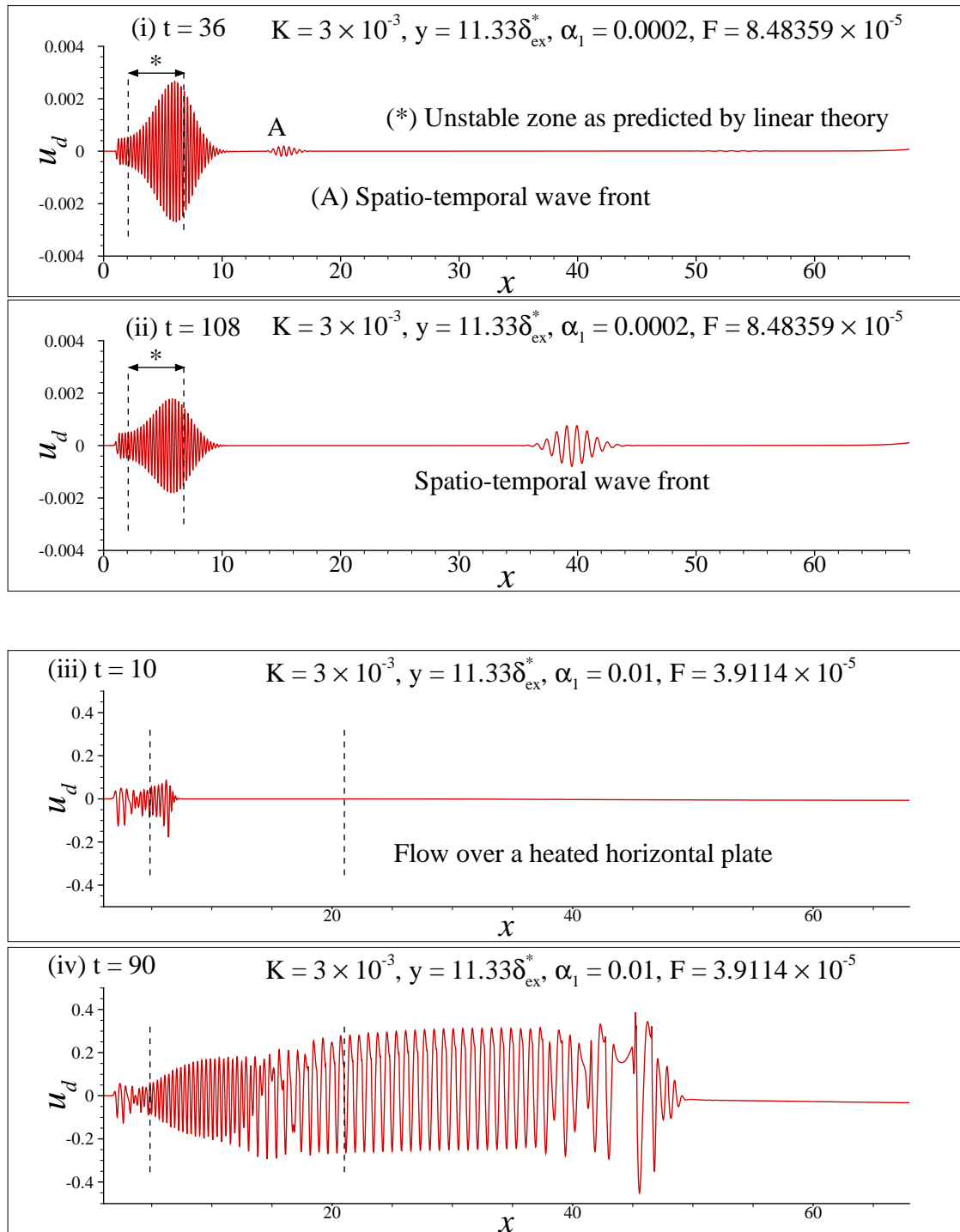


Figure 1e Disturbance streamwise velocity  $u_d$  plotted at indicated times after the onset of excitation at  $y = 11.33\delta_{ex}^*$  for indicated amplitudes and frequencies of excitation for flow past a semi-infinite heated horizontal flat plate, where prescribed wall temperature is varied as  $T_w(x) \simeq x^{-1/2}$  to obtain equilibrium flow as Schneider's similarity profiles. Here,  $\delta_{ex}^*$  indicates the displacement thickness at the exciter location.

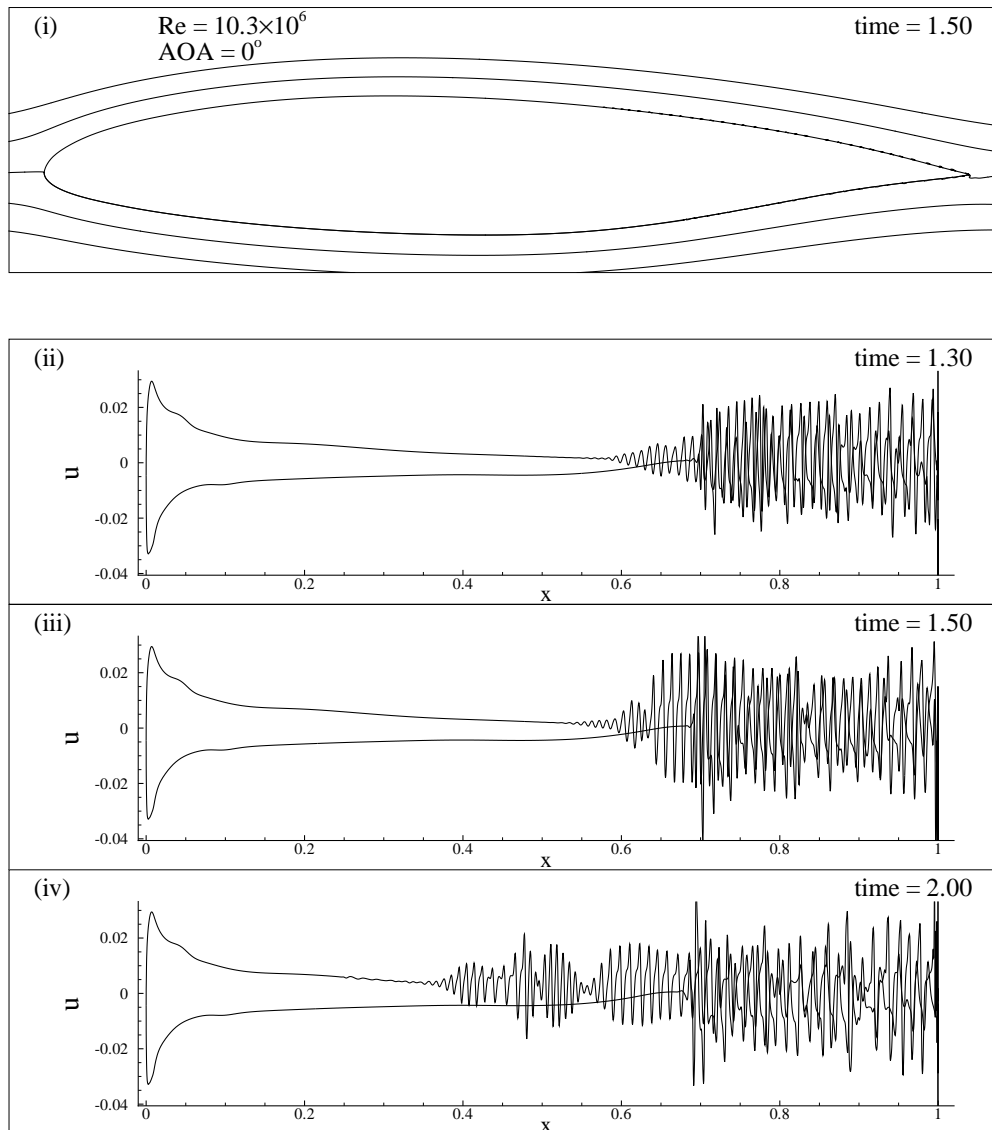


Figure 1f (i) Streamline contours are shown for flow past a NLF SHM-1 aerofoil at zero angle of attack for  $Re = 10.3 \times 10^6$  and (ii) to (iv) variations of azimuthal component of velocity at the second  $\eta = const.$  ( $j=2$ ) line shown over the surface of the aerofoil at different instants.

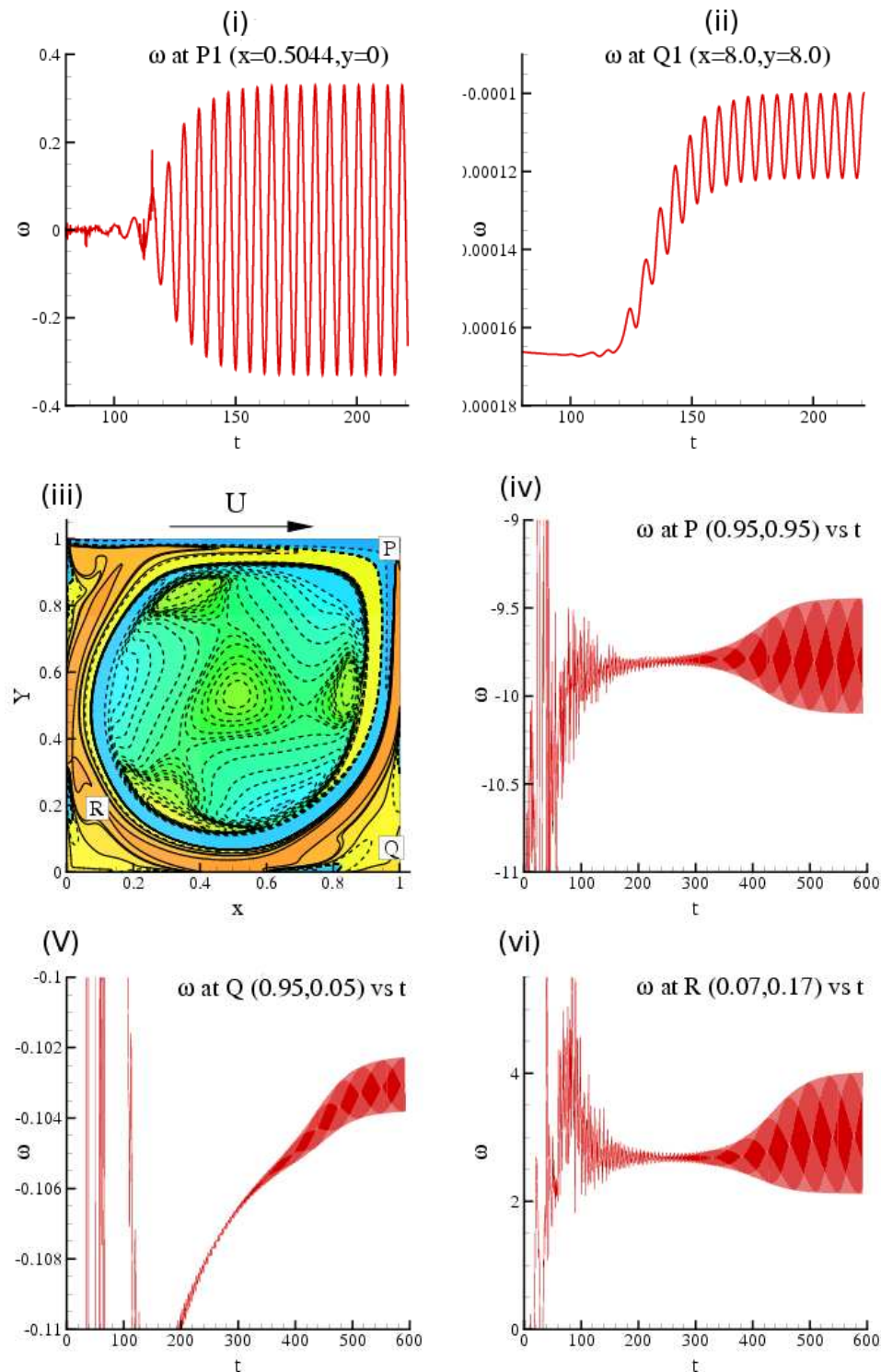


Figure 2a Time variation of computed vorticity shown for flow past a circular cylinder for  $Re = 100$  at a point (i) on the wake center line,  $P1(x=0.5044, y=0.0)$  and a point (ii) offset from the wake center line,  $Q1(x=8.0, y=8.0)$ . The center of the unit diameter cylinder is located at origin. (iii) Computed vorticity field of flow inside a square lid-driven cavity for  $Re = 8500$  shown at  $t = 550.0$ . In frames (iv) to (vi), time variation of vorticity at P, Q and R are shown, respectively.

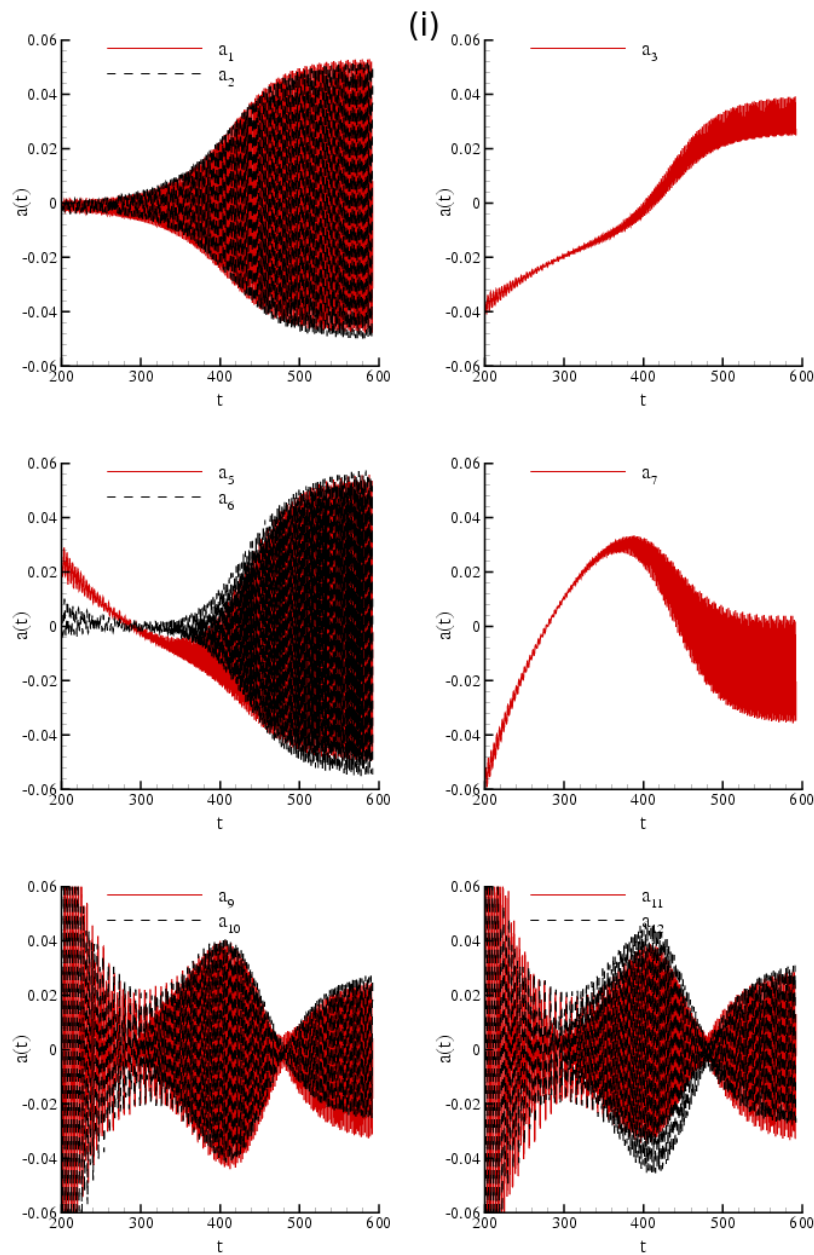


Figure 2b(i) Time-dependent POD amplitude functions for the LDC flow for  $Re = 8500$  during  $t = 201-592$ . The modes  $(a_1, a_2)$ ;  $(a_5, a_6)$ ;  $(a_9, a_{10})$  and  $(a_{11}, a_{12})$  form pairs, with  $a_3$  and  $a_7$  as the T1-modes. Modes  $a_9$  to  $a_{12}$  are anomalous type T2-modes, which do not follow time variation given by Stuart-Landau equations.

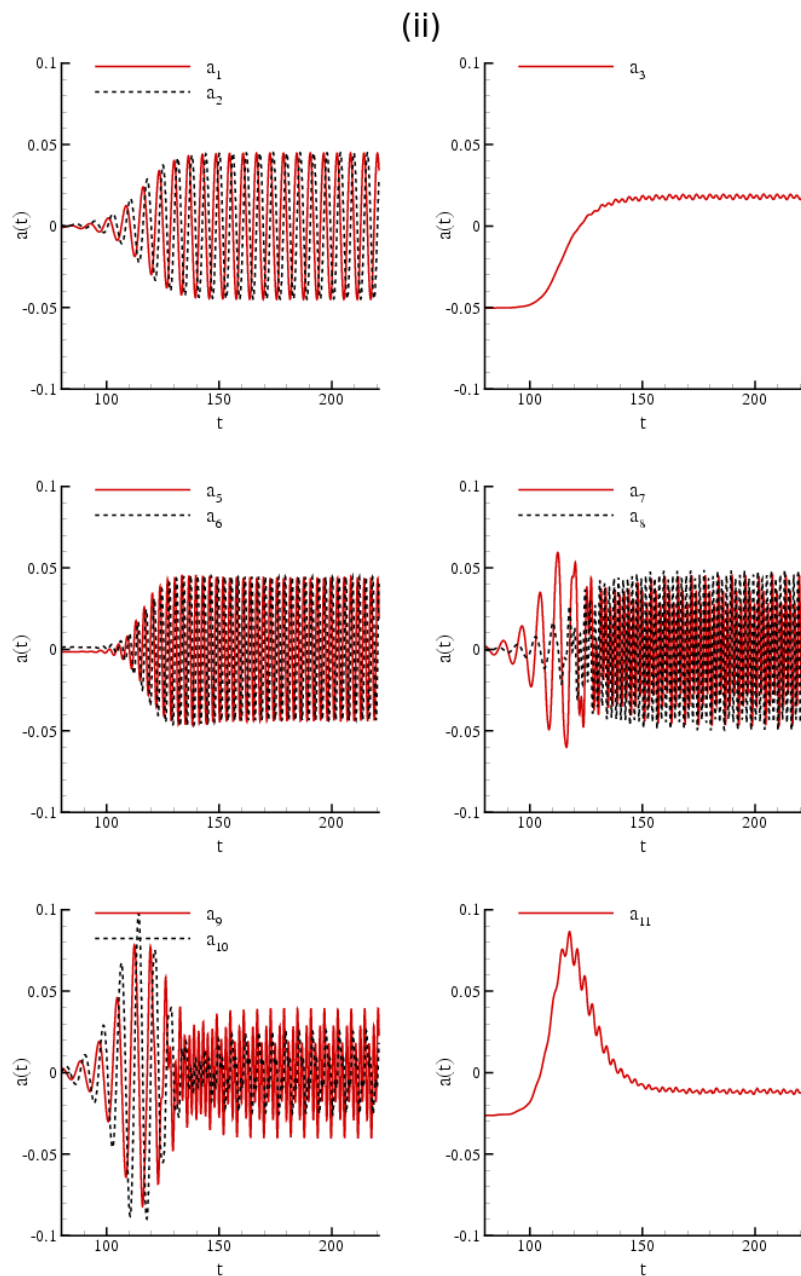


Figure 2b(ii) Time-dependent POD amplitudes for flow past a circular cylinder for  $Re = 100$  during  $t = 200-350$ . The modes  $(a_1, a_2)$ ;  $(a_5, a_6)$ ;  $(a_7, a_8)$  and  $(a_9, a_{10})$  form pairs, with  $a_3$  and  $a_{11}$  as T1-modes. Modes  $a_5 - a_{10}$  are anomalous T2-modes, which do not follow the time variation given by StuartLandau equations.

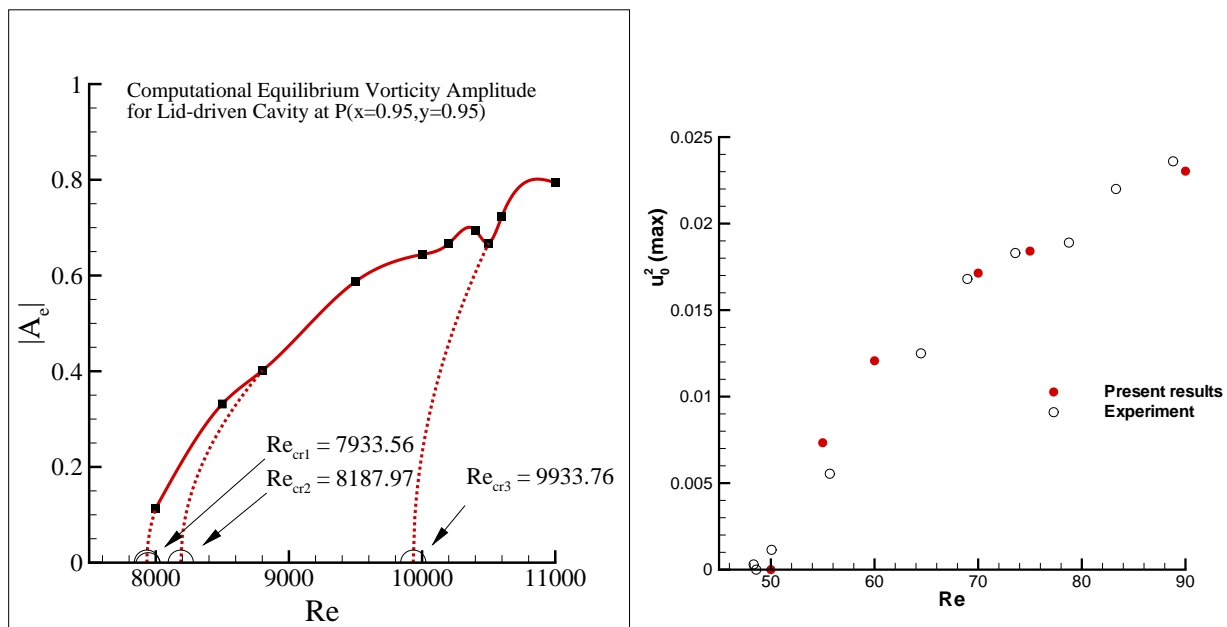


Figure 3a Left frame shows, equilibrium amplitude of the computed vorticity variation plotted against  $Re$  for the flow in LDC with critical Reynolds numbers for the point  $P$  ( $x=0.95$ ,  $y=0.95$ ). Right frame shows, experimental data (blank circle) from Strykowski (1986) and computations (filled circle) showing variation of amplitude of fluctuating streamwise velocity component with Reynolds number. Data were obtained at 8 diameter behind the cylinder in the wake. Presented computed data have been normalized with the experimental value for  $Re = 70$ .

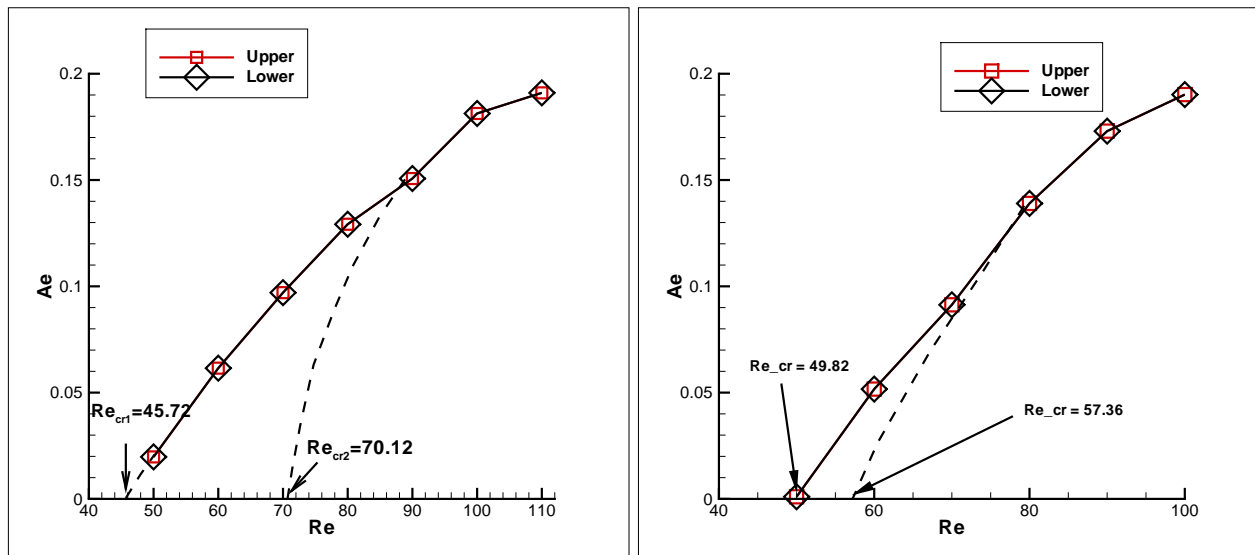


Figure 3b  $Ae$  vs  $Re$  curve is shown for two side-by-side cylinder arrangement with distance between upper and lower cylinders for  $s^* = 3.4d^*$  and  $s^* = 2.5d^*$  in left and right frames, respectively.

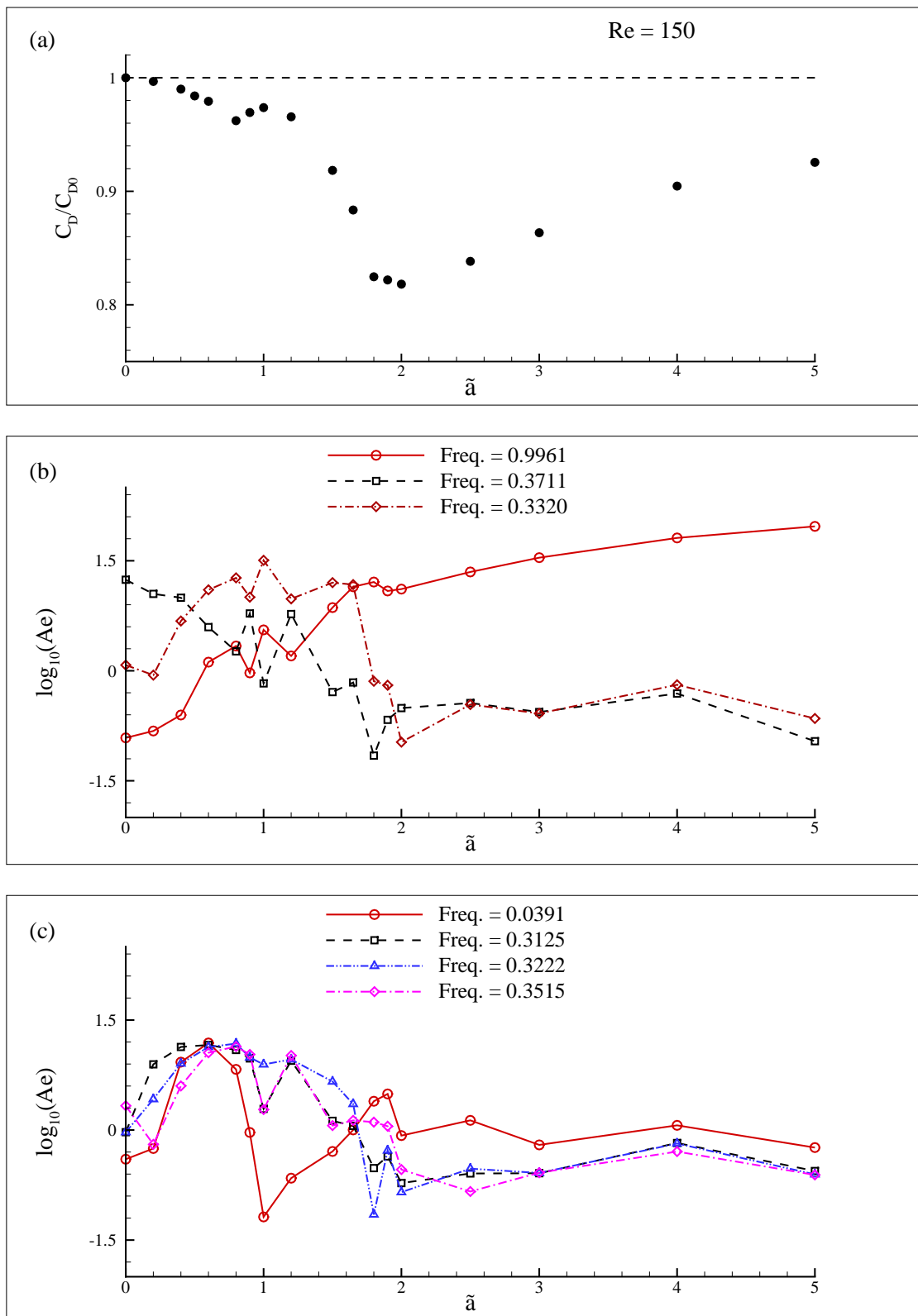


Figure 4 Normalized drag coefficient variation with amplitude of rotary oscillation for the case of  $Re = 150$ ,  $\tilde{a} = 2$ ,  $S_f = \pi/2$ . Frames 4b and 4c show variations of different important frequencies present in the time series of drag variation with respect to forcing amplitude  $\tilde{a}$ .

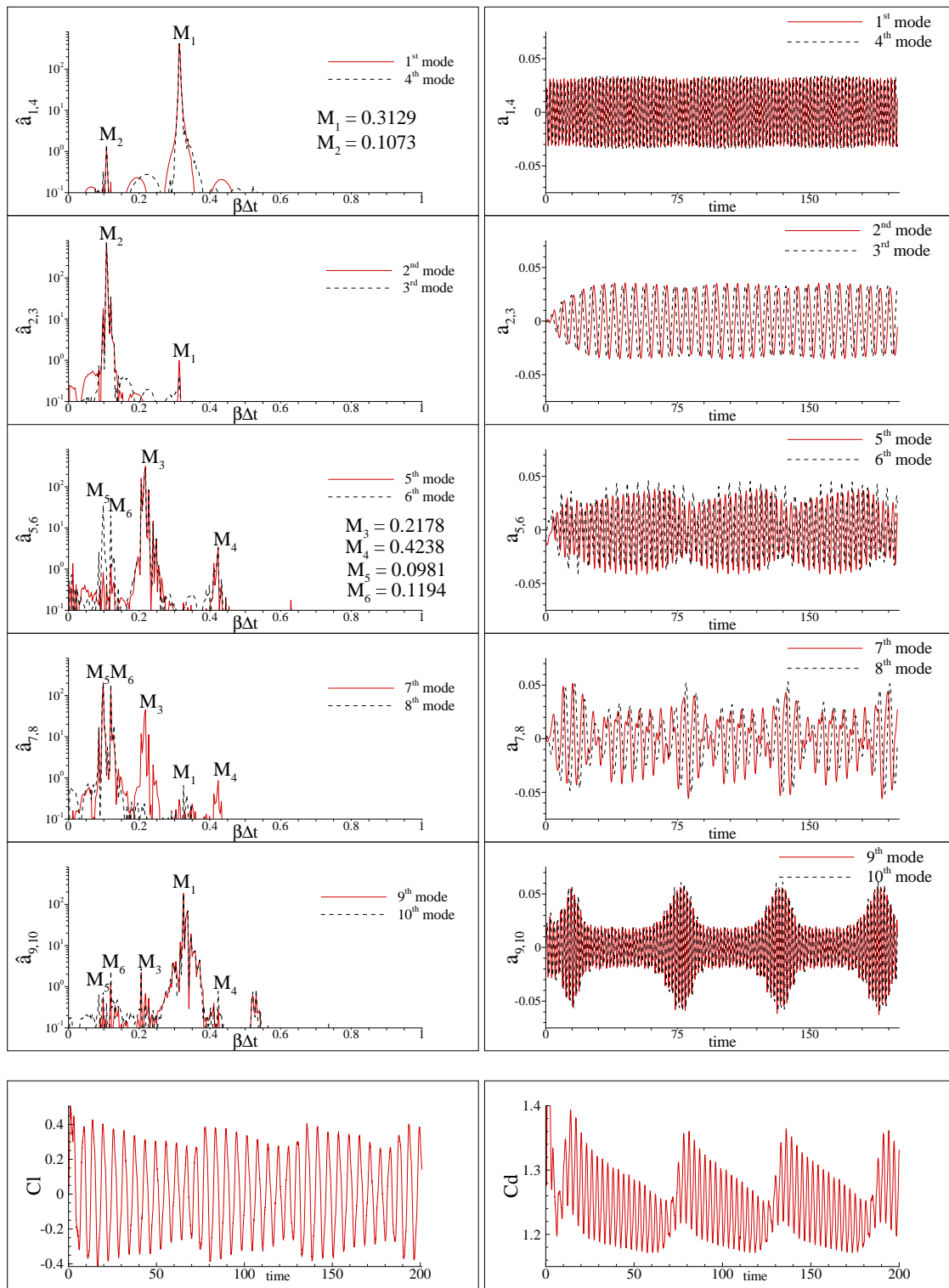


Figure 5a Time dependent amplitude function  $a_j(t)$  of first ten POD modes for the case of flow past a cylinder performing rotary oscillations for  $Re = 150$ ,  $\tilde{a} = 0.8$ ,  $S_f = \pi/2$  are shown in the right column as a function of time while the left column shows corresponding FFT. Bottom two frames shows variation of lift and drag coefficient with time.

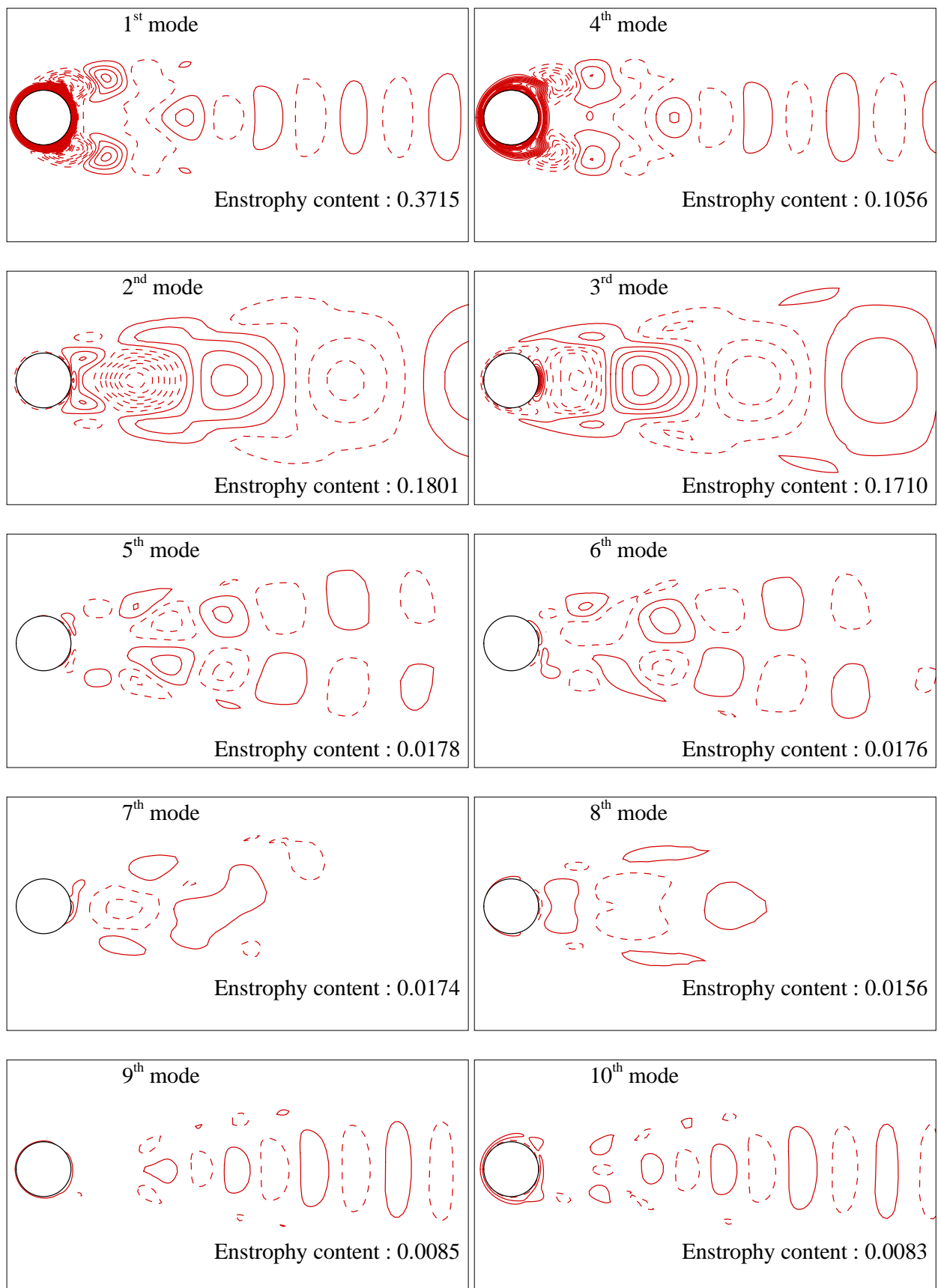


Figure 5b Contours of eigenfunctions  $\phi_j(x, y)$  of first ten POD modes for the case of flow past a cylinder performing rotary oscillations for  $Re = 150$ ,  $\tilde{a} = 0.8$ ,  $S_f = \pi/2$  are shown along with the individual enstrophy content.

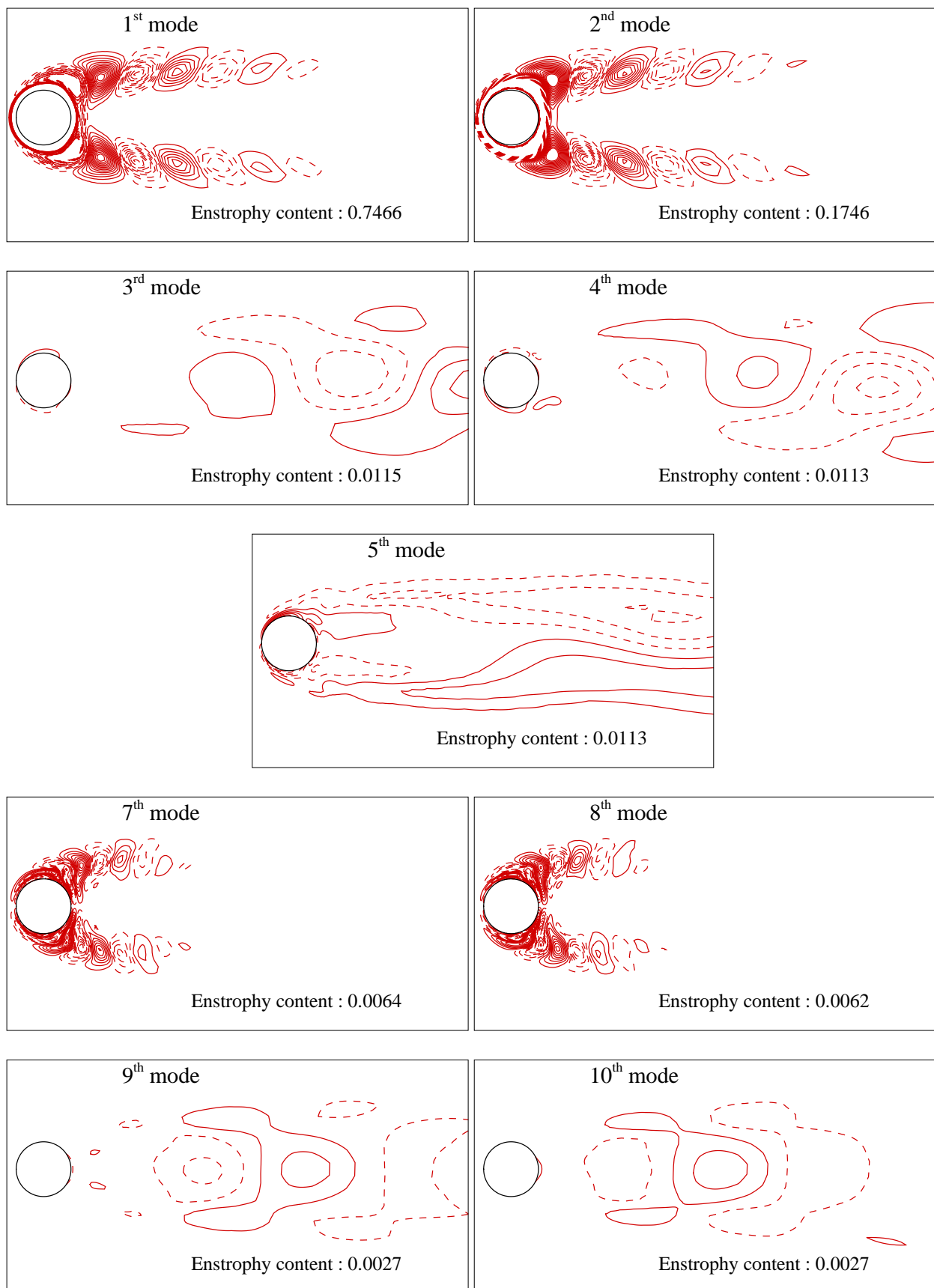


Figure 5c Contours of eigenfunctions  $\phi_j(x, y)$  of first ten POD modes for the case of flow past a cylinder performing rotary oscillations for  $Re = 150$ ,  $\tilde{a} = 2$ ,  $S_f = \pi/2$  are shown along with the individual enstrophy content.

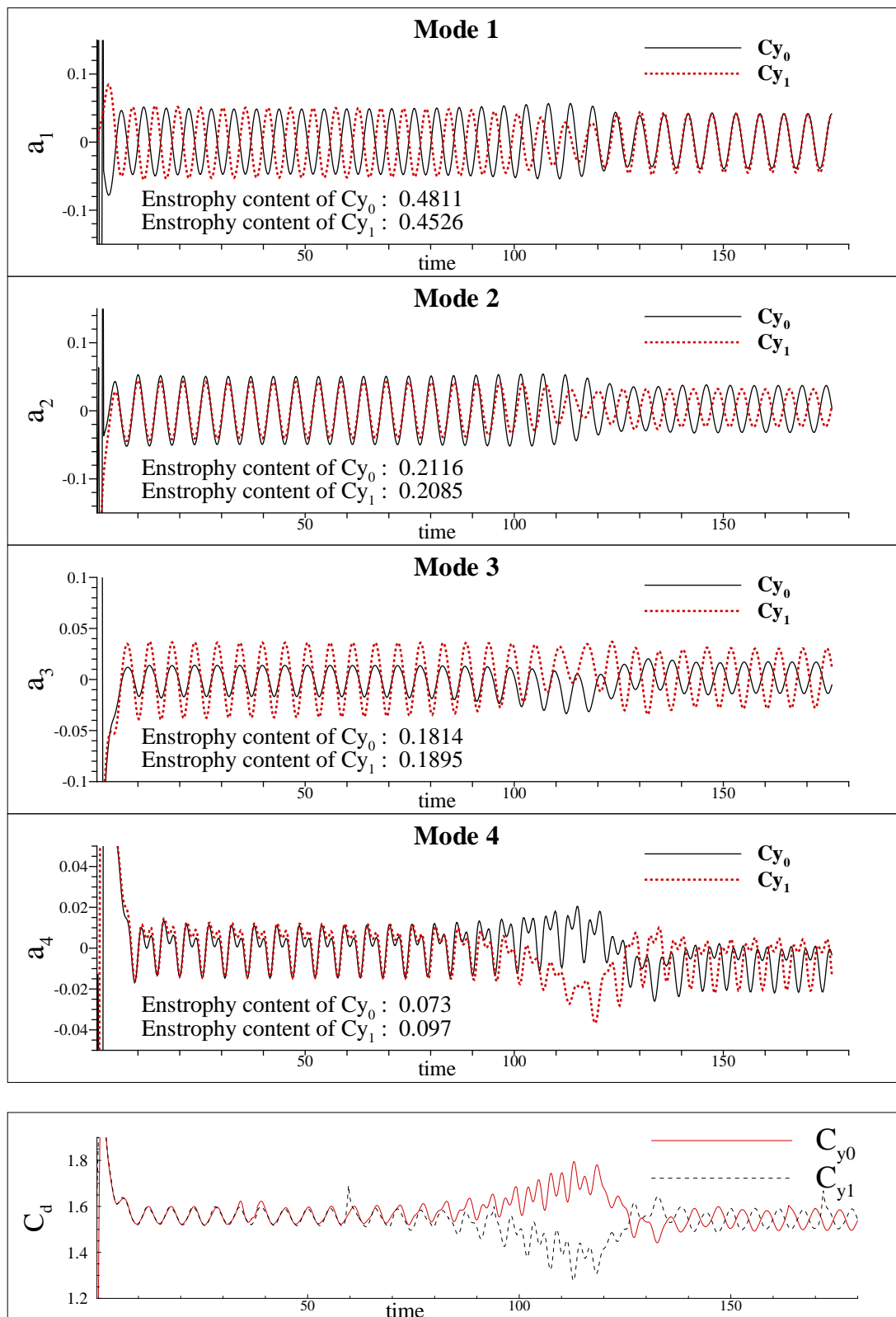


Figure 6 Time variation of first four POD amplitude functions are shown for the case of  $s^* = 2.5d^*$  along with the individual enstrophy content. Bottom frame shows time variation of drag coefficient for the two cylinders.

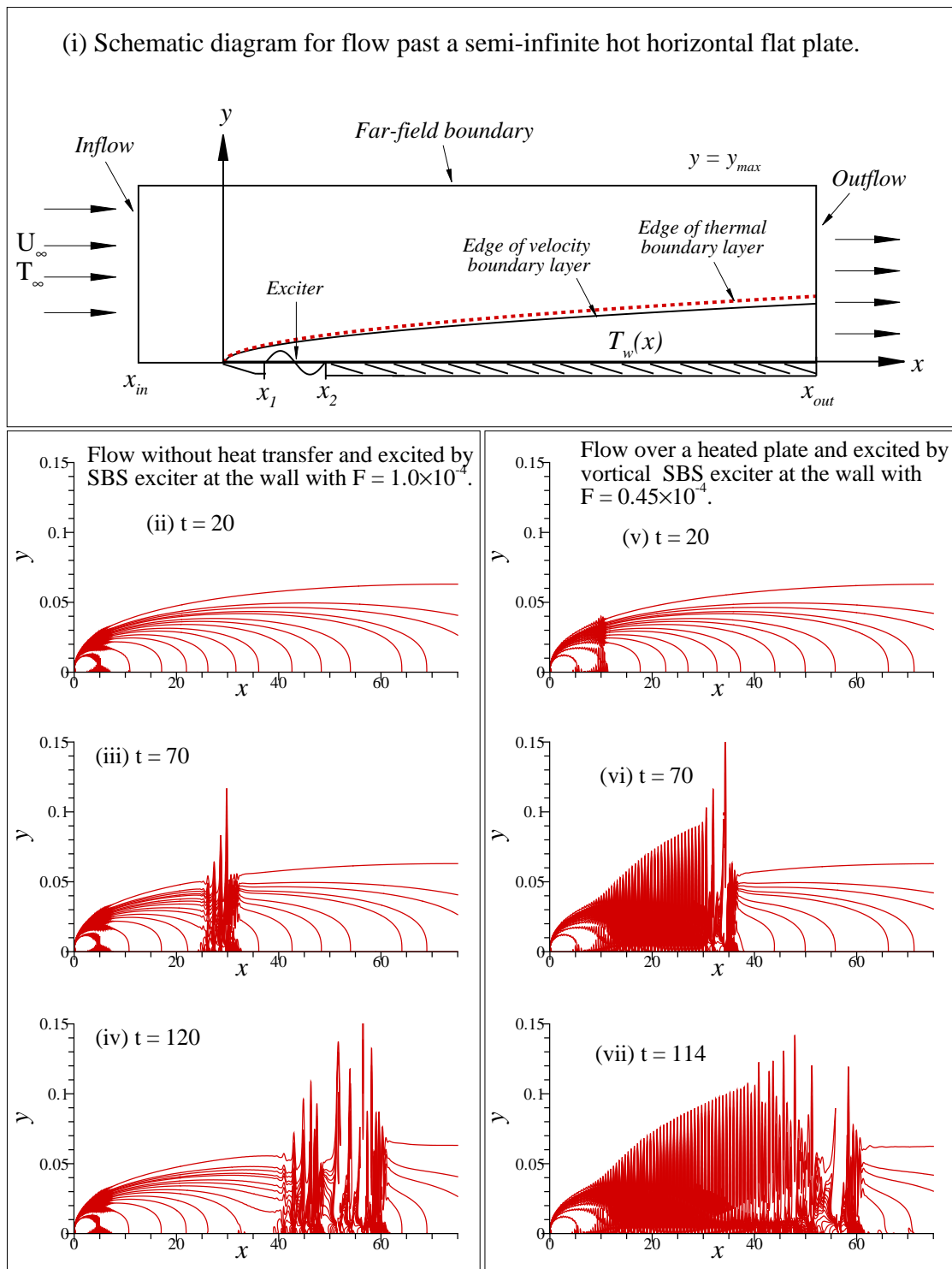


Figure 7 (i) Schematic diagram of flow past a semi-infinite heated flat plate is shown. The flow is excited by a simultaneous blowing-suction (SBS) exciter strip indicated. (ii)-(iv) Vorticity contours at indicated times after the onset of SBS excitation are shown plotted for flow past a semi-infinite horizontal flat plate without heat transfer. (v)-(vii) Vorticity contours at indicated times after the onset of SBS excitation are shown for flow past a semi-infinite heated horizontal flat plate. Here, prescribed wall temperature is varied as  $T_w(x) \simeq x^{-1/2}$  so that the equilibrium flow follows Schneider's similarity profile.

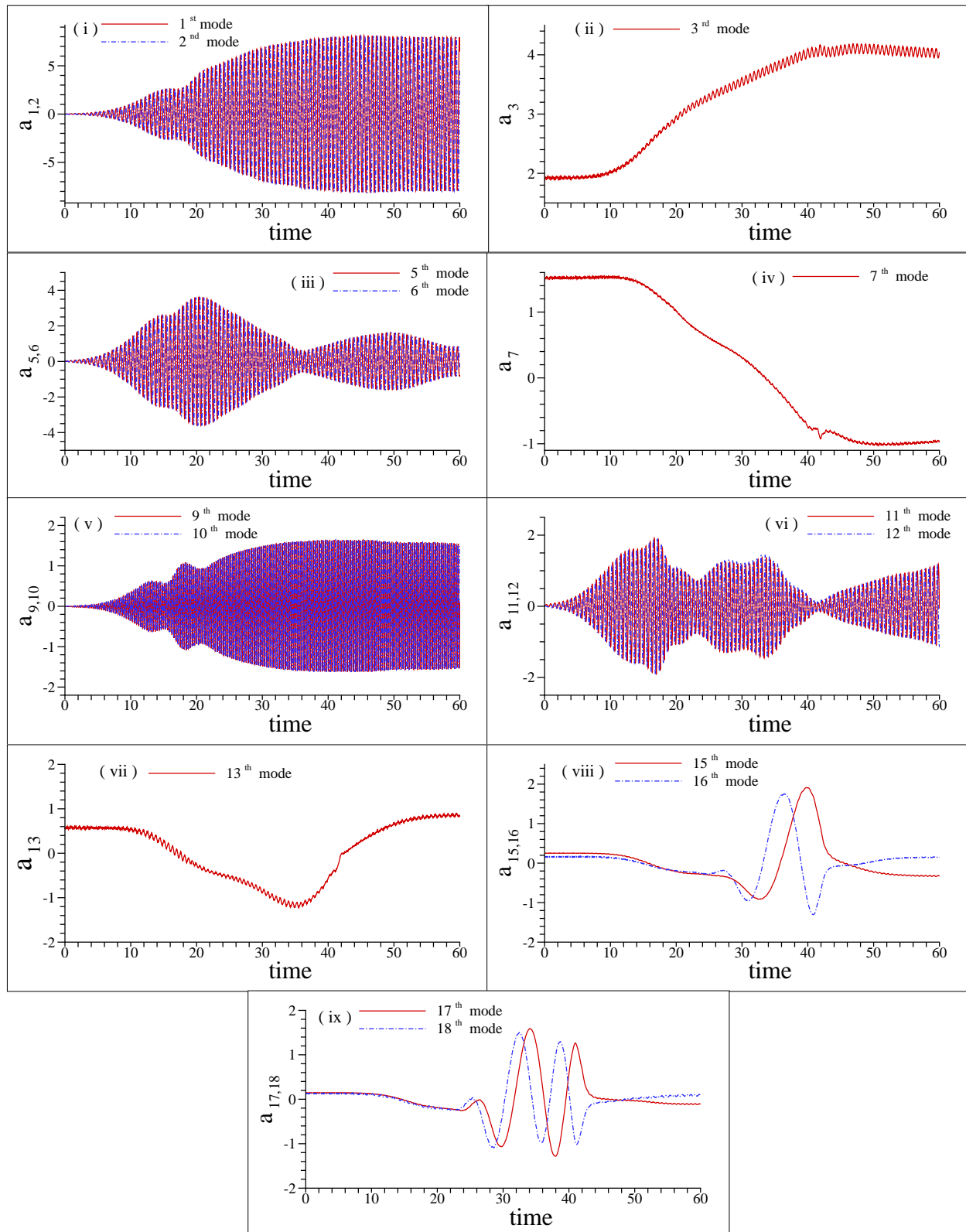


Figure 8 Time dependent amplitude function  $a_j(t)$  of first eighteen POD modes for zero-pressure gradient flow over semi-infinite flat-plate with wall-excitation are shown plotted as a function of time. The pair-forming modes are shown together in frames, as indicated.

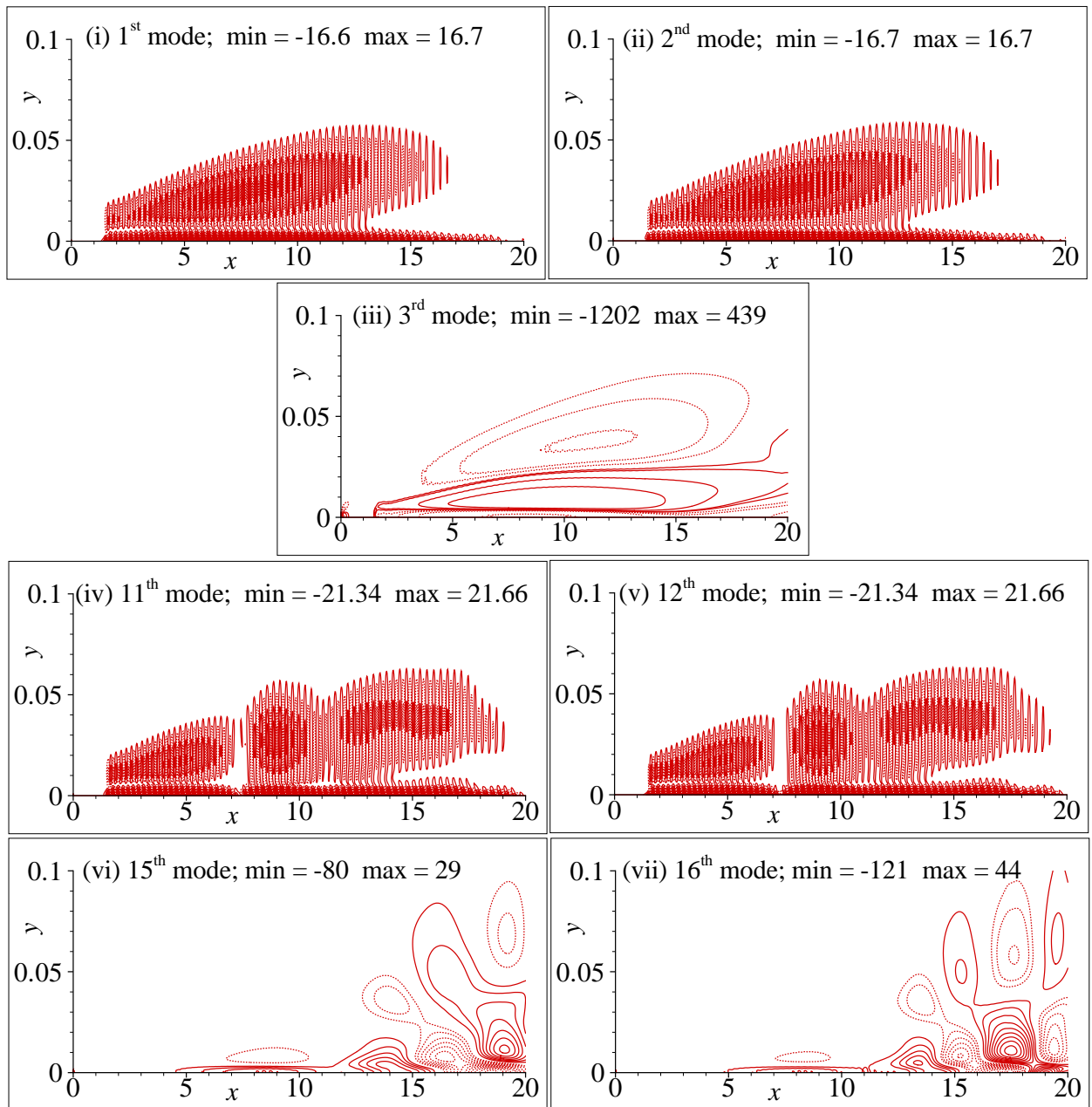


Figure 9 Contours of eigenfunctions  $\phi_j(x,y)$  corresponding to the first eighteen POD modes for zero-pressure gradient flow over semi-infinite flat-plate with wall-excitation are shown.

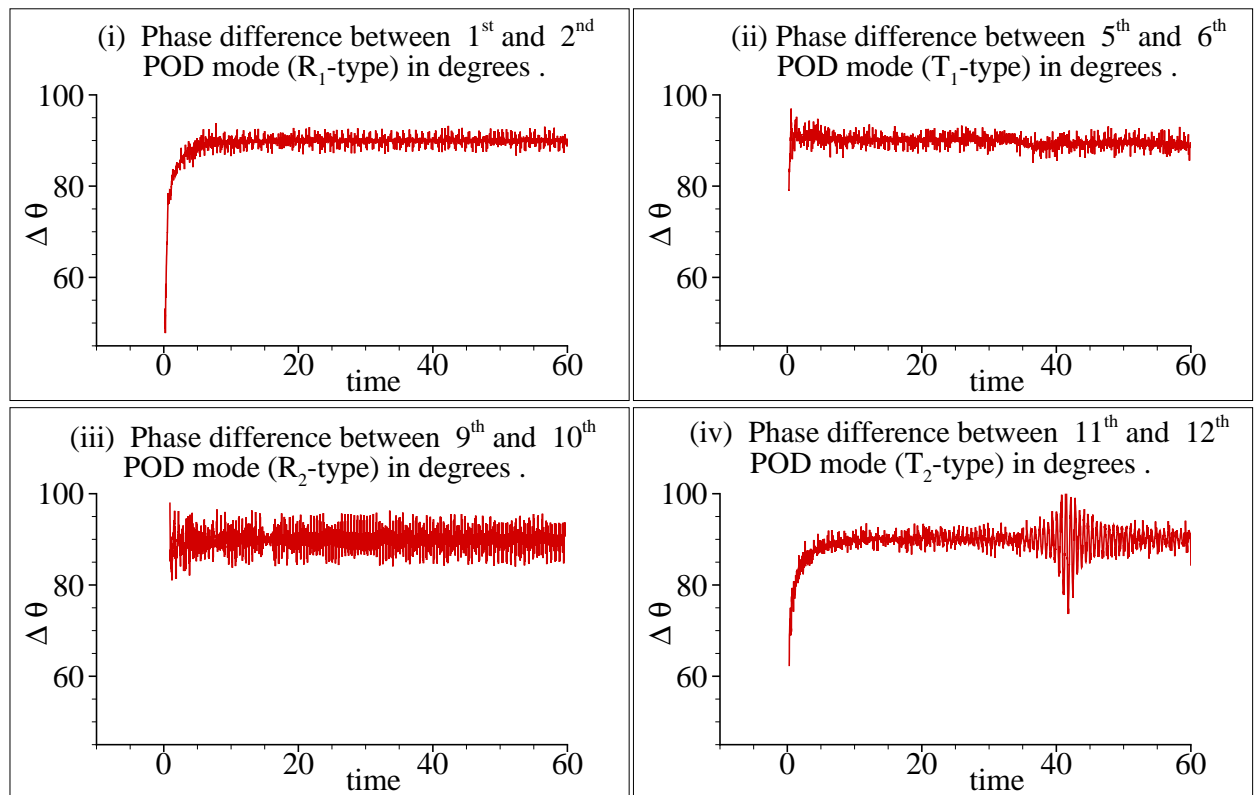


Figure 10 Phase difference  $\Delta\theta$  between four different indicated mode pairs are shown as a function of time for zero-pressure gradient flow over semi-infinite flat-plate with wall-excitation.

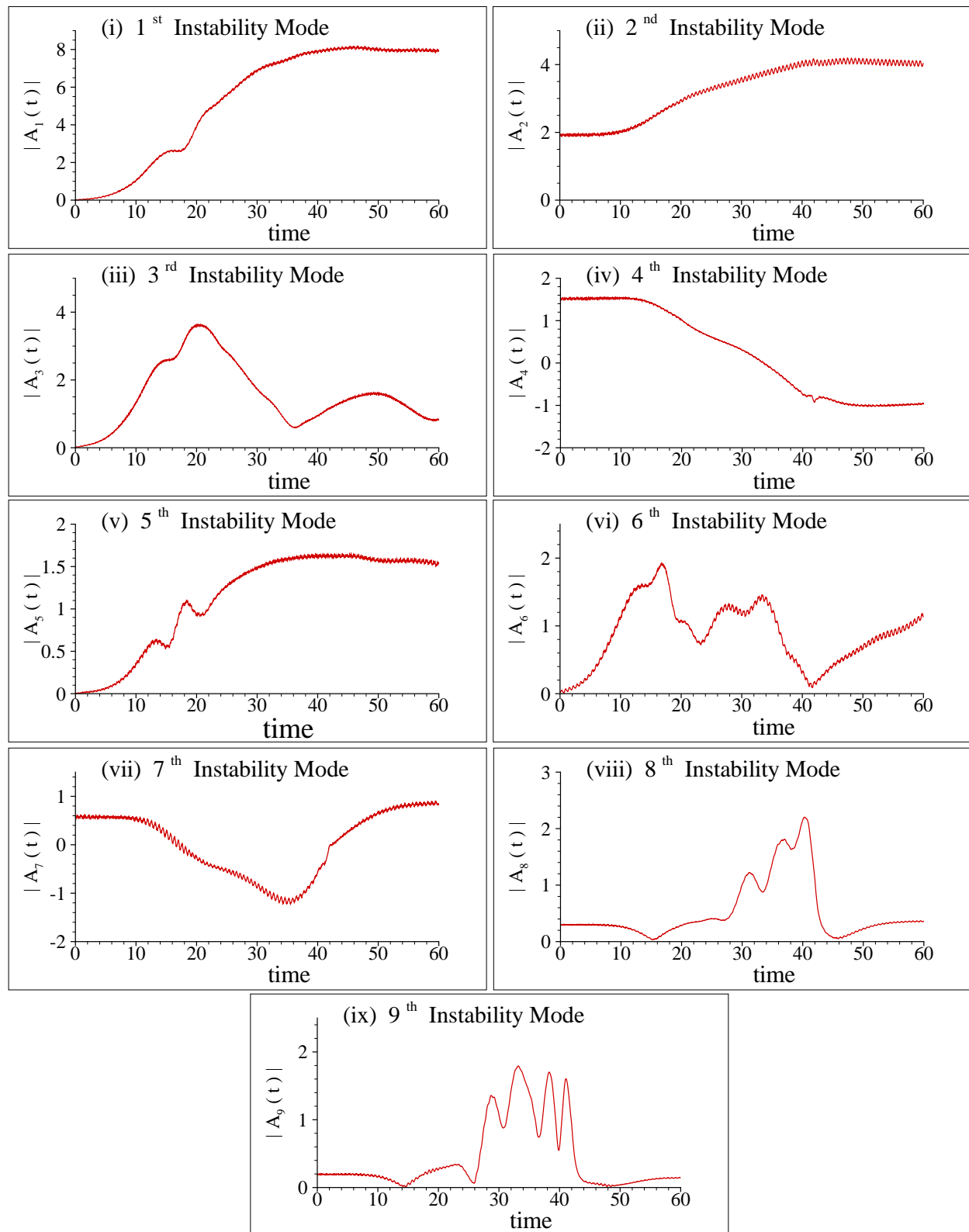


Figure 11 Modulus of amplitude function  $|A_j(t)|$  of indicated instability modes are shown as a function of time for zero-pressure gradient flow over semi-infinite flat-plate with wall-excitation.

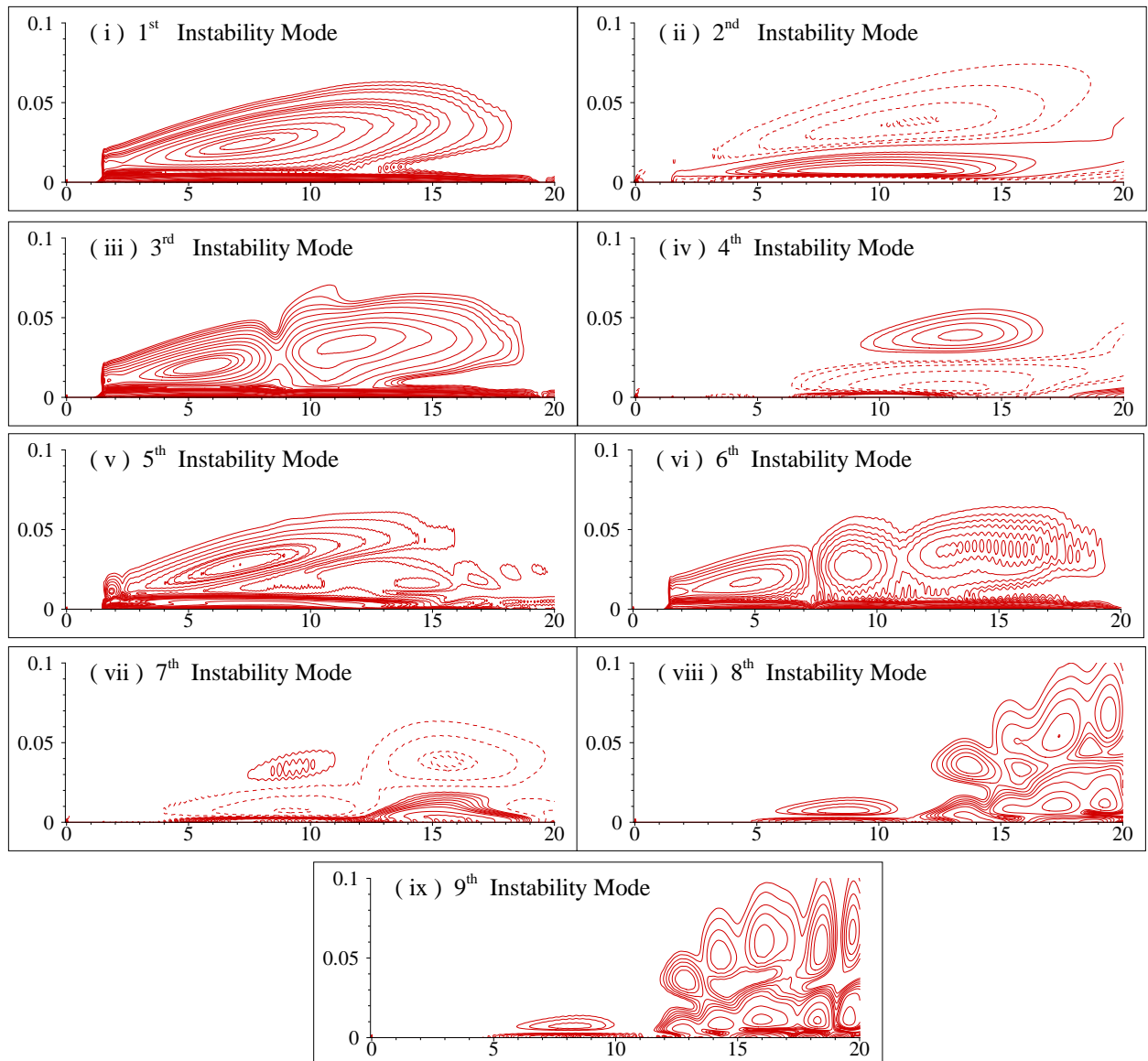


Figure 12 Modulus of space dependent function  $|f_j(\vec{X})|$  of indicated instability modes are shown as a function of time for zero-pressure gradient flow over semi-infinite flat-plate with wall-excitation.

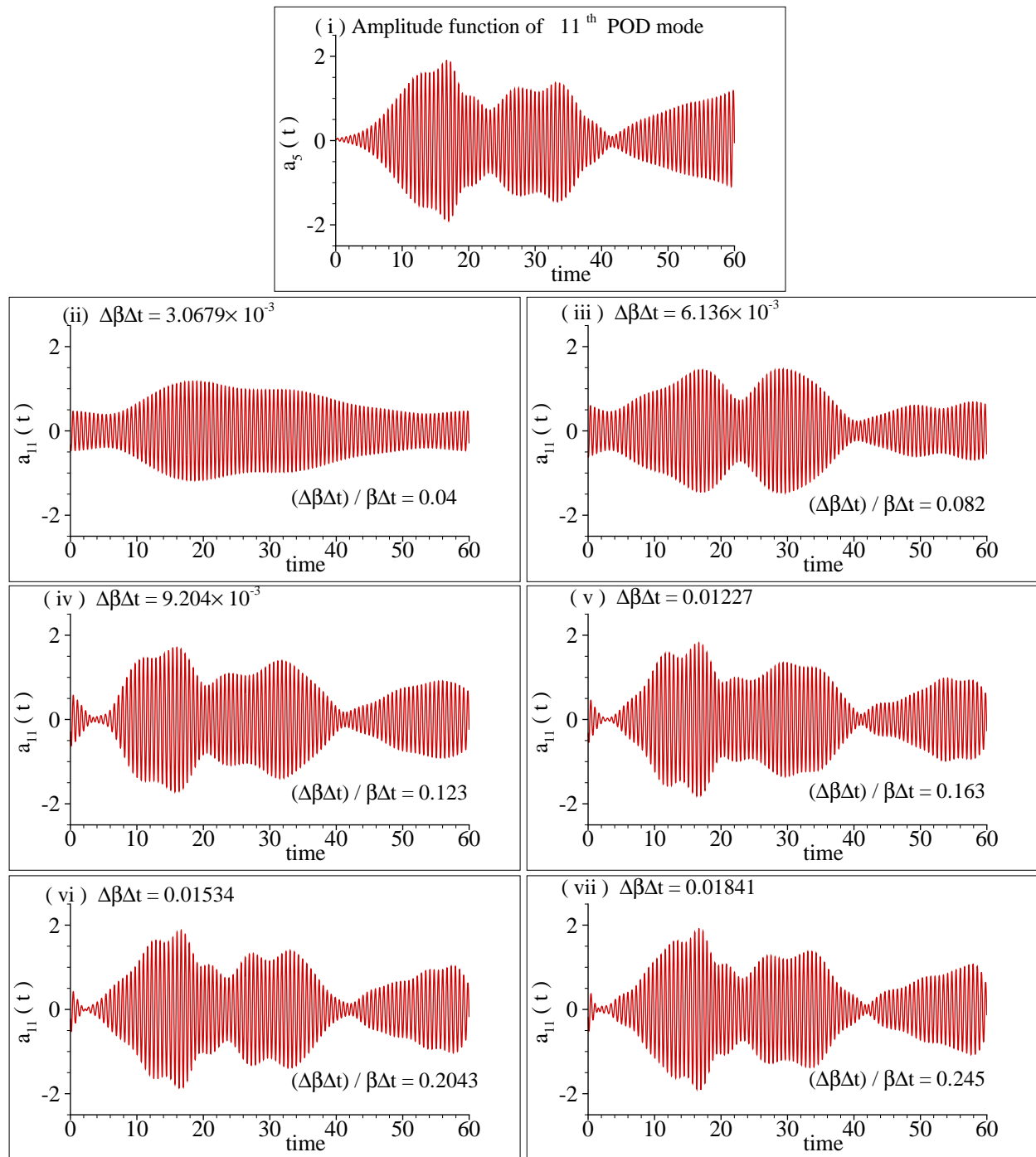


Figure 13 Reconstructed signals of  $a_{11}(t)$  with indicated frequency-band about the peak at  $\beta\Delta t = 7.234 \times 10^{-2}$  are shown in frames (ii) to (vii). The original signal  $a_{11}(t)$  is shown in the top frame.

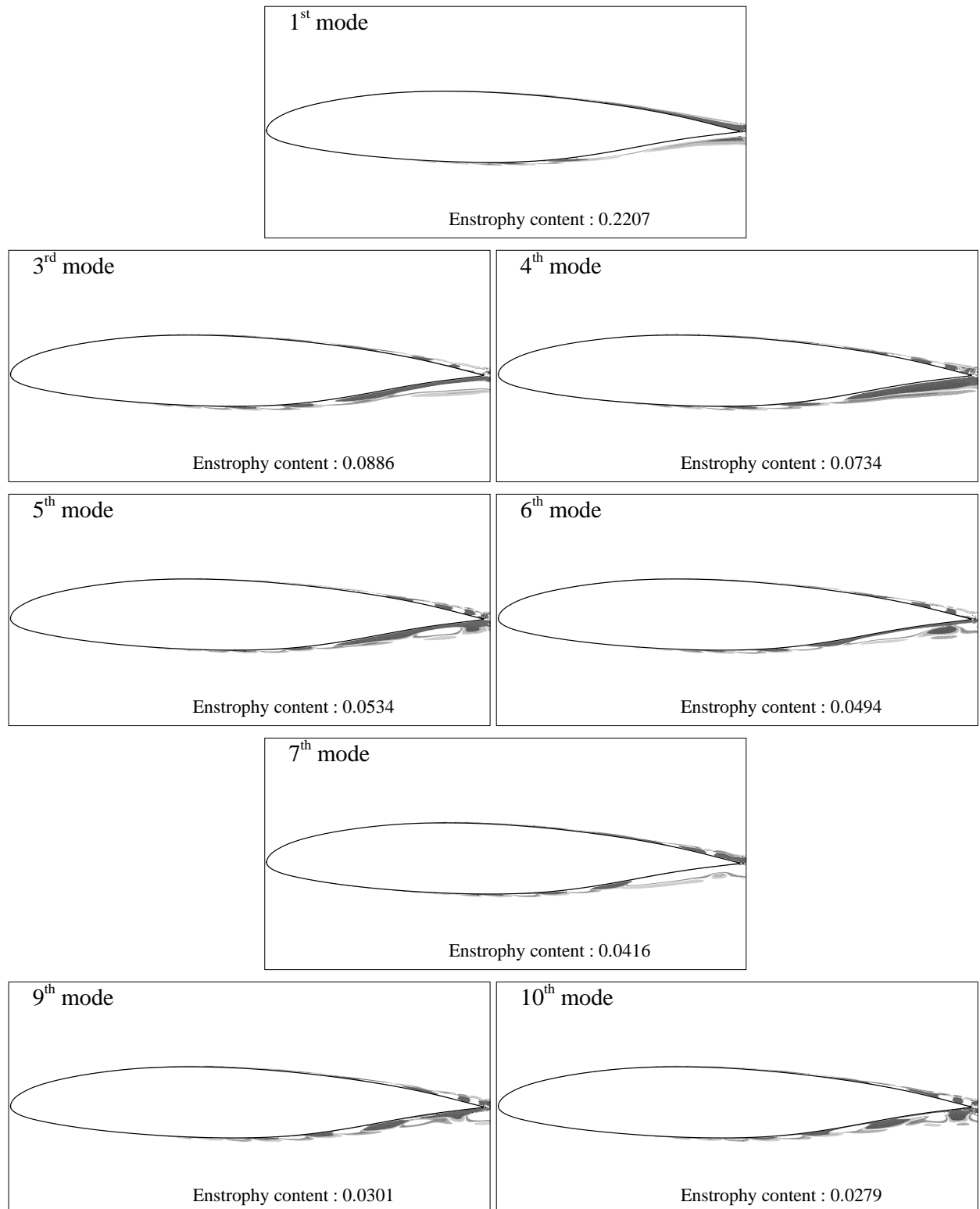


Figure 14a Contours of eigenfunctions  $\phi_j(x, y)$  corresponding to first ten POD modes for flow over SHM-1 aerofoil at  $Re = 10.3 \times 10^6$  and  $AOA = 0^\circ$  are shown.

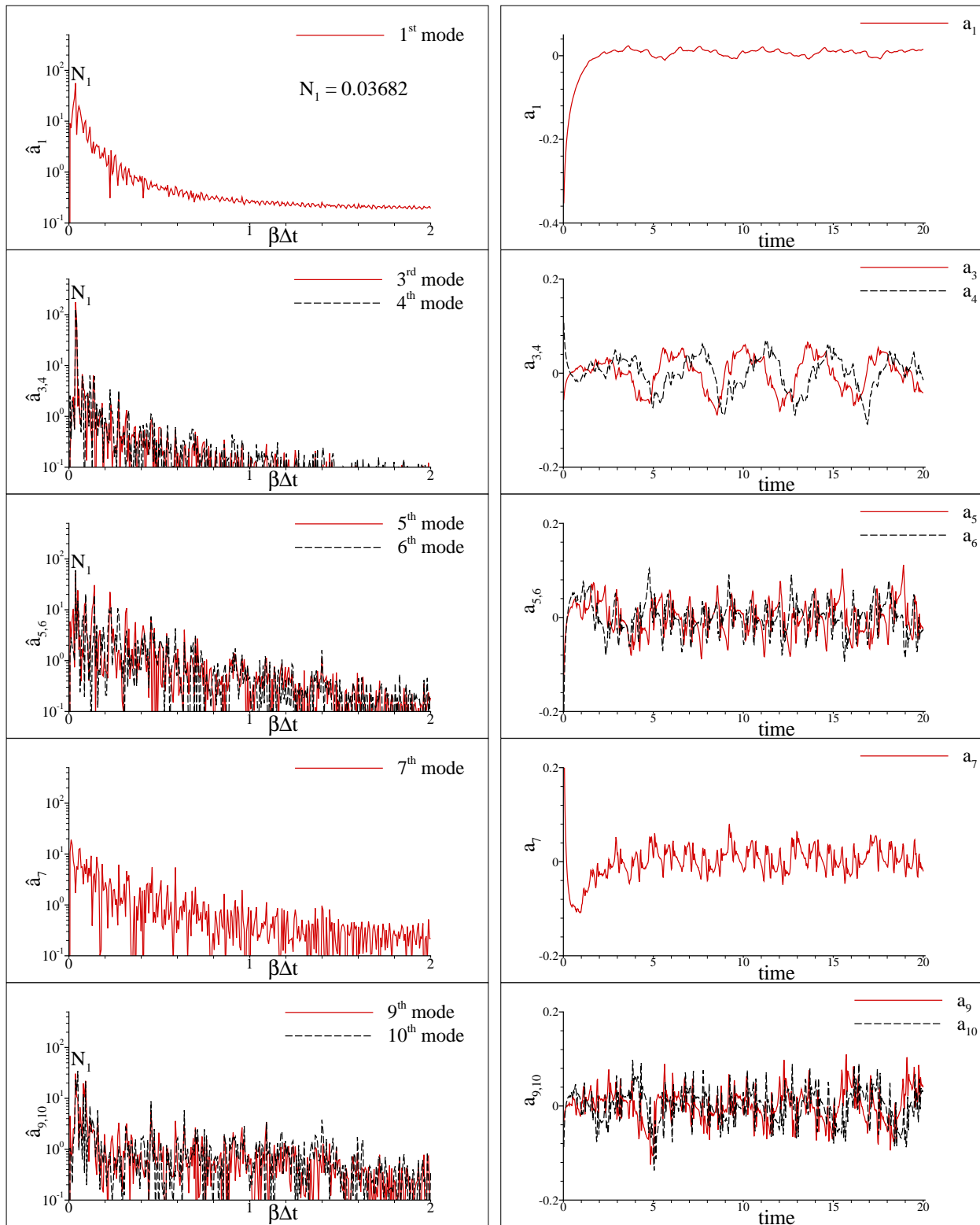


Figure 14b Time dependent amplitude function  $a_j(t)$  of first ten POD modes for flow over SHM-1 aerofoil for  $Re = 10.3 \times 10^6$  and  $AOA = 0^\circ$  are shown as a function of time in right column frames. FFT of the respective  $a_j(t)$  are shown in the left column frames. The pair-forming modes are shown together.

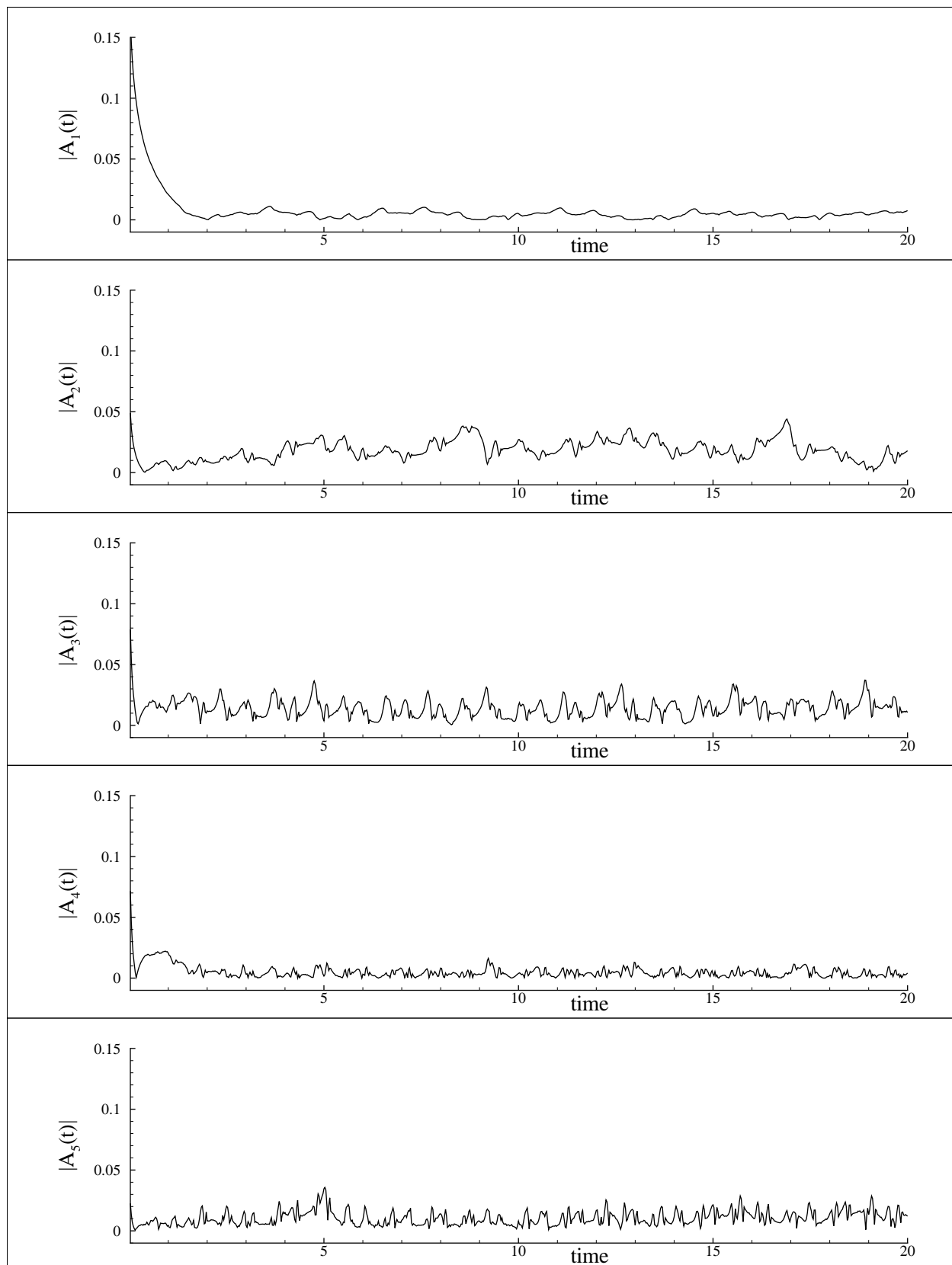


Figure 14c Modulus of amplitude function  $|A_j(t)|$  of the indicated instability modes are shown as a function of time for flow over SHM-1 aerofoil at  $Re = 10.3 \times 10^6$  and  $AOA = 0^\circ$ .

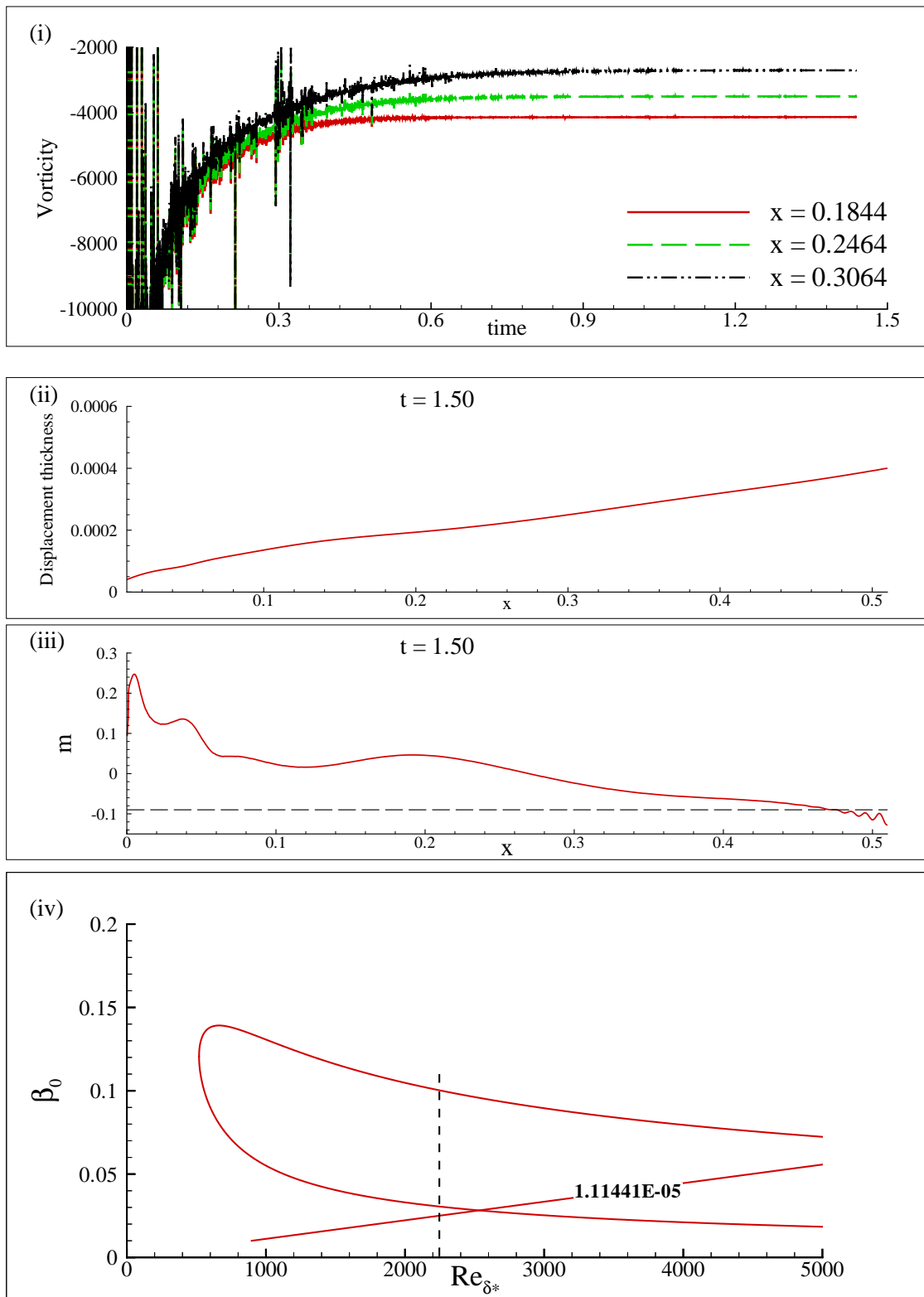


Figure 15a (i) Variation of vorticity with time at indicated  $x$ -coordinates on top surface of SHM-1 aerofoil before applying SBS excitation; Variation of (ii) displacement thickness and (iii) steady flow separation parameter  $m = \frac{x}{U_e} \frac{\partial U_e}{\partial x}$  are shown on the top surface of SHM-1 aerofoil at  $t = 1.5$  and (iv) frequency of wall-excitation  $F = 1.11441 \times 10^{-5}$  is shown on the neutral curve based on linear stability theory. Vertical dotted line corresponds to Reynolds number at the exciter  $Re_{\delta^*} = 2246.8$ .

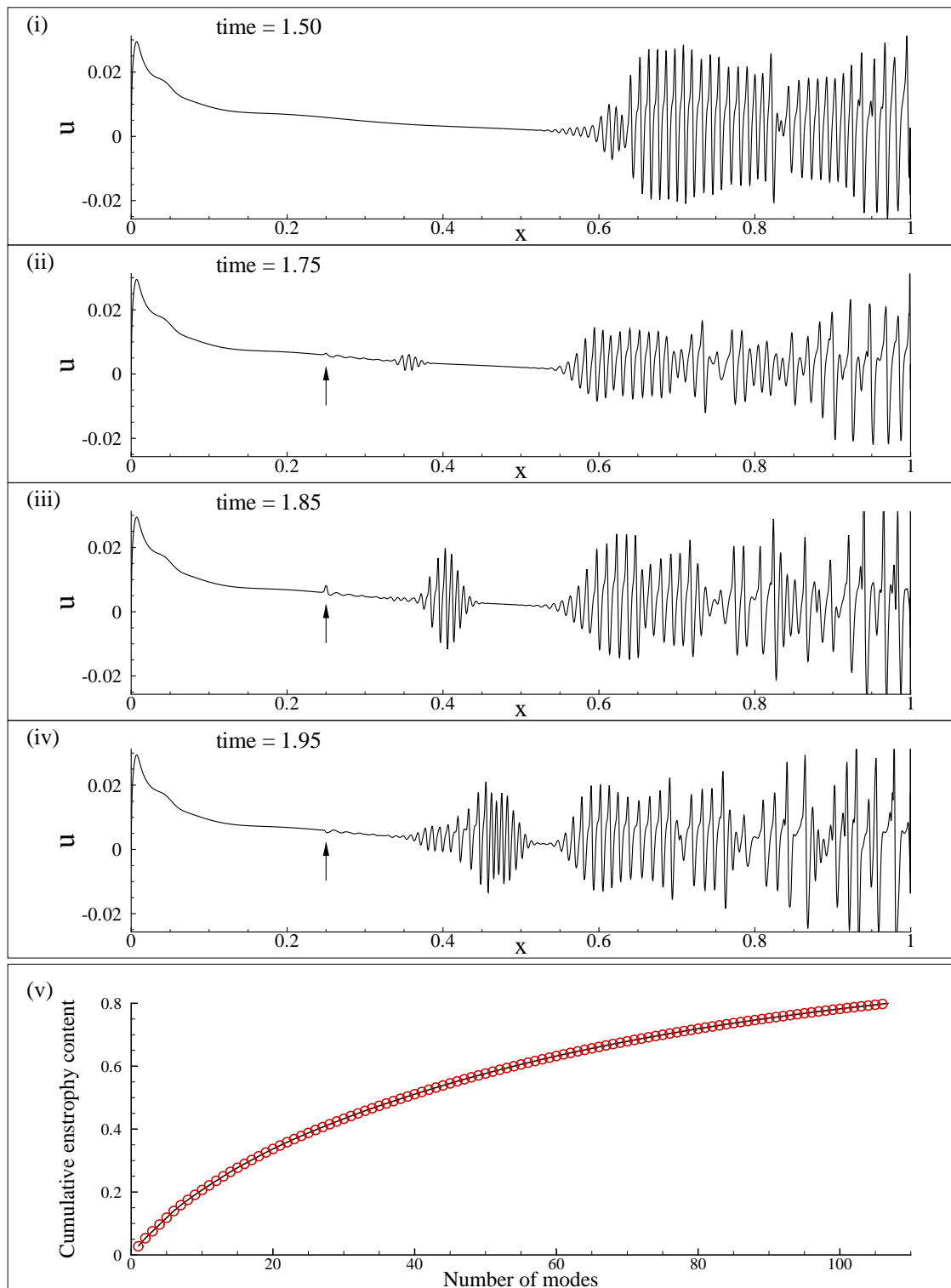


Figure 15b Variation of the azimuthal component of the velocity ( $u$ ) at a distance of  $1.242 \times 10^{-6}$  from the surface of the SHM-1 aerofoil is shown for the top surface at the indicated time instants in frames (i)-(iv). Wall-excitation is started from  $t = 1.50$  onwards and the vertical arrow in frames (ii) to (iv) indicates location of the exciter and (v) Variation of cumulative enstrophy content with number of modes for the case of flow past SHM-1 aerofoil with wall-excitation as explained in the text.

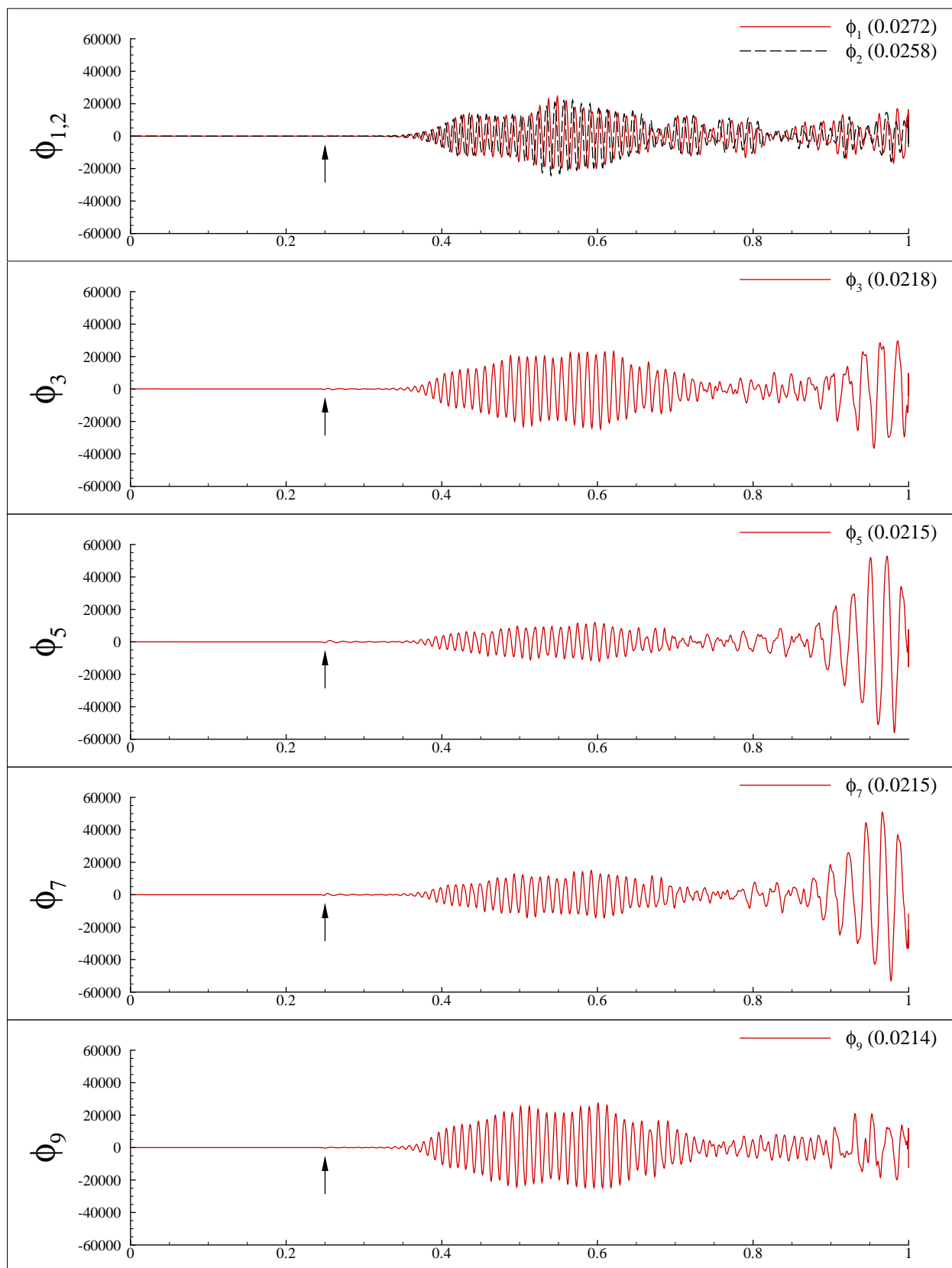


Figure 15c Variation of eigenfunctions  $\phi_j(x, y)$  corresponding to the first nine POD modes on the top surface of SHM-1 aerofoil at a distance of  $1.2465 \times 10^{-5}$  from the surface are shown plotted for the excitation case as explained in the text.

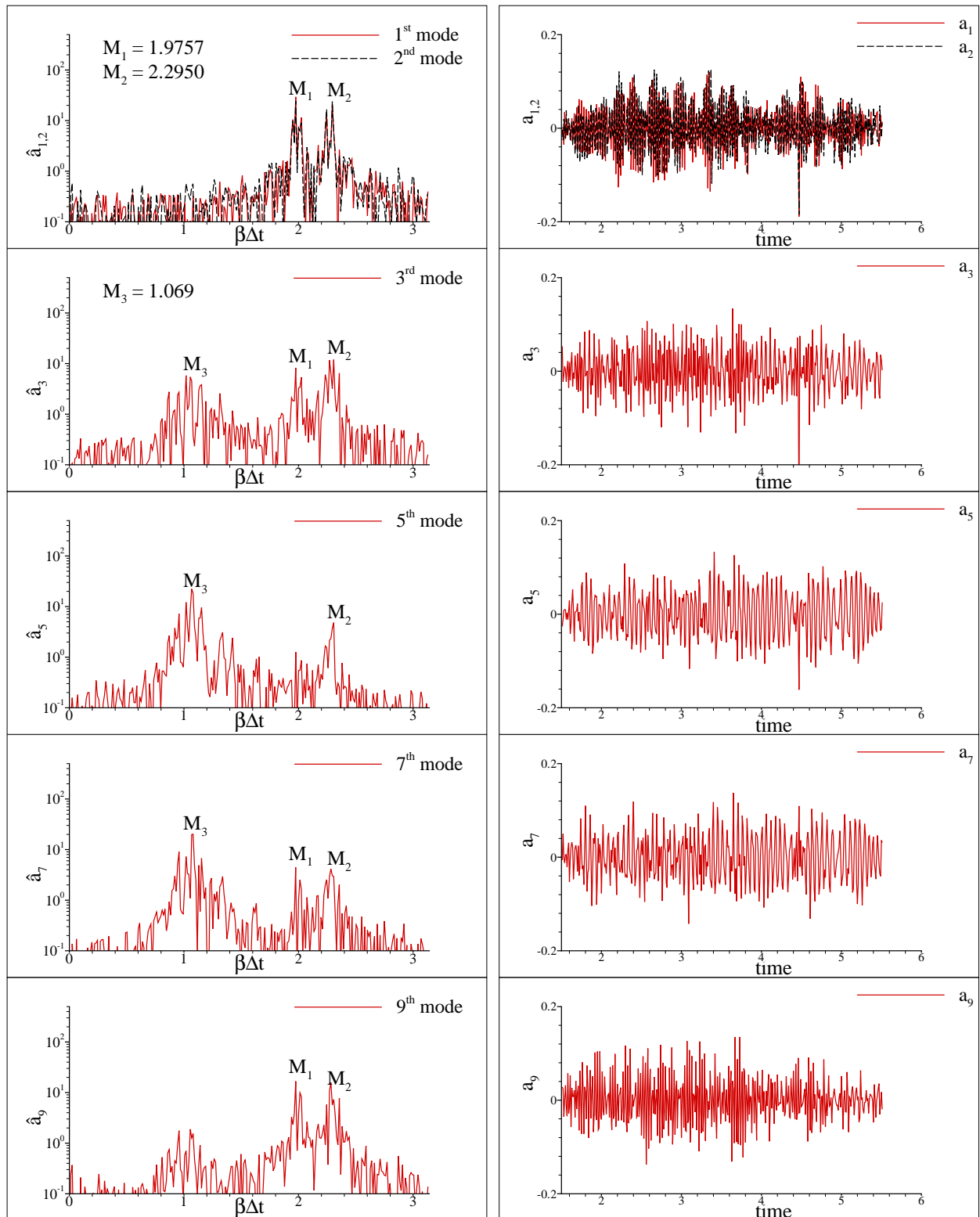


Figure 15d Time dependent amplitude function  $a_j(t)$  of first nine POD modes for flow over SHM-1 aerofoil with wall-excitation as explained in the text are shown plotted as a function of time in right column frames. FFT of the respective  $a_j(t)$  are shown in the left column frames.

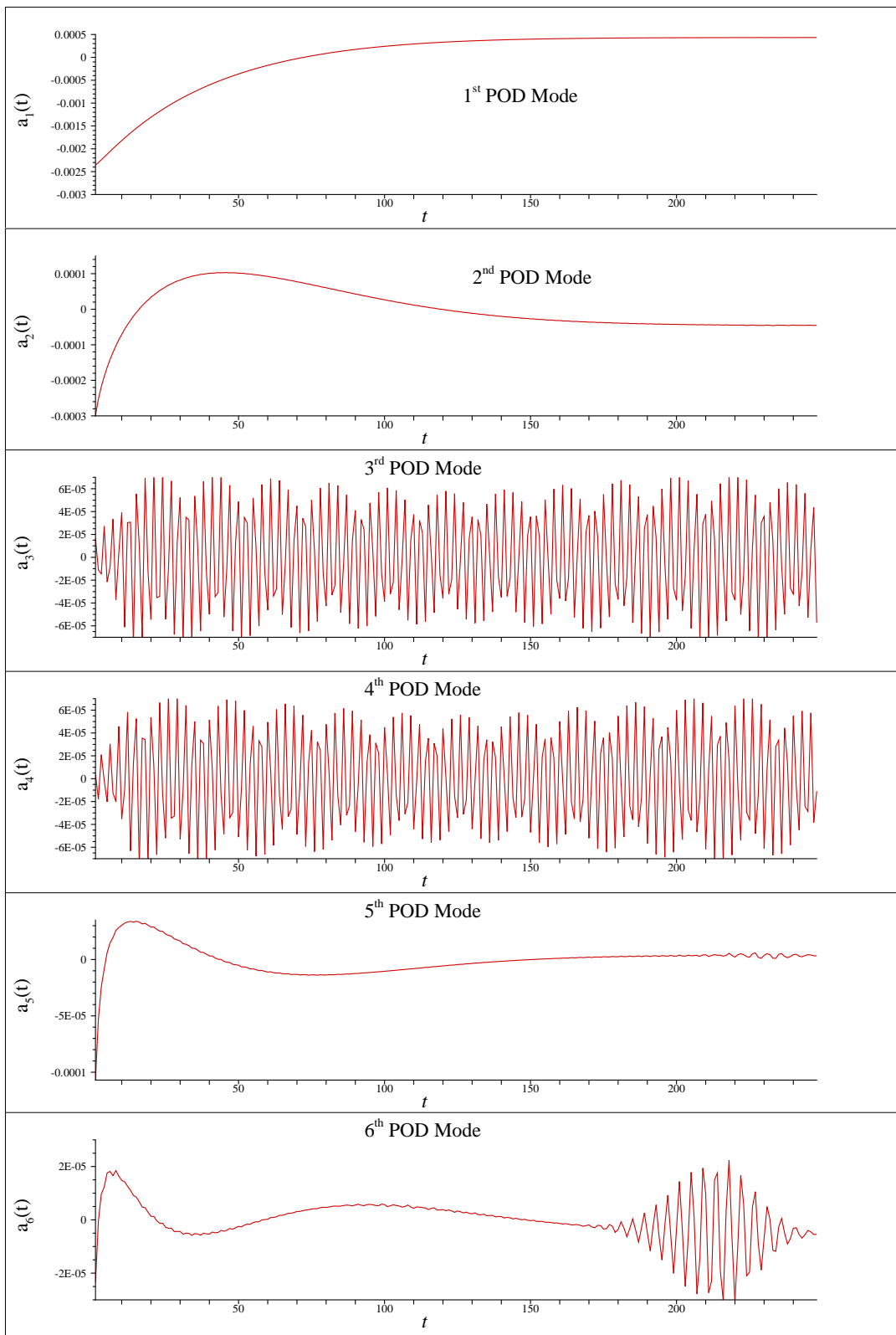


Figure 16 Time dependent amplitude function  $a_j(t)$  of temperature disturbance for first six POD modes for flow past a heated semi-infinite flat plate subjected to SBS strip excitation. The buoyancy and excitation parameters for this case are given in Figure 1e(i).

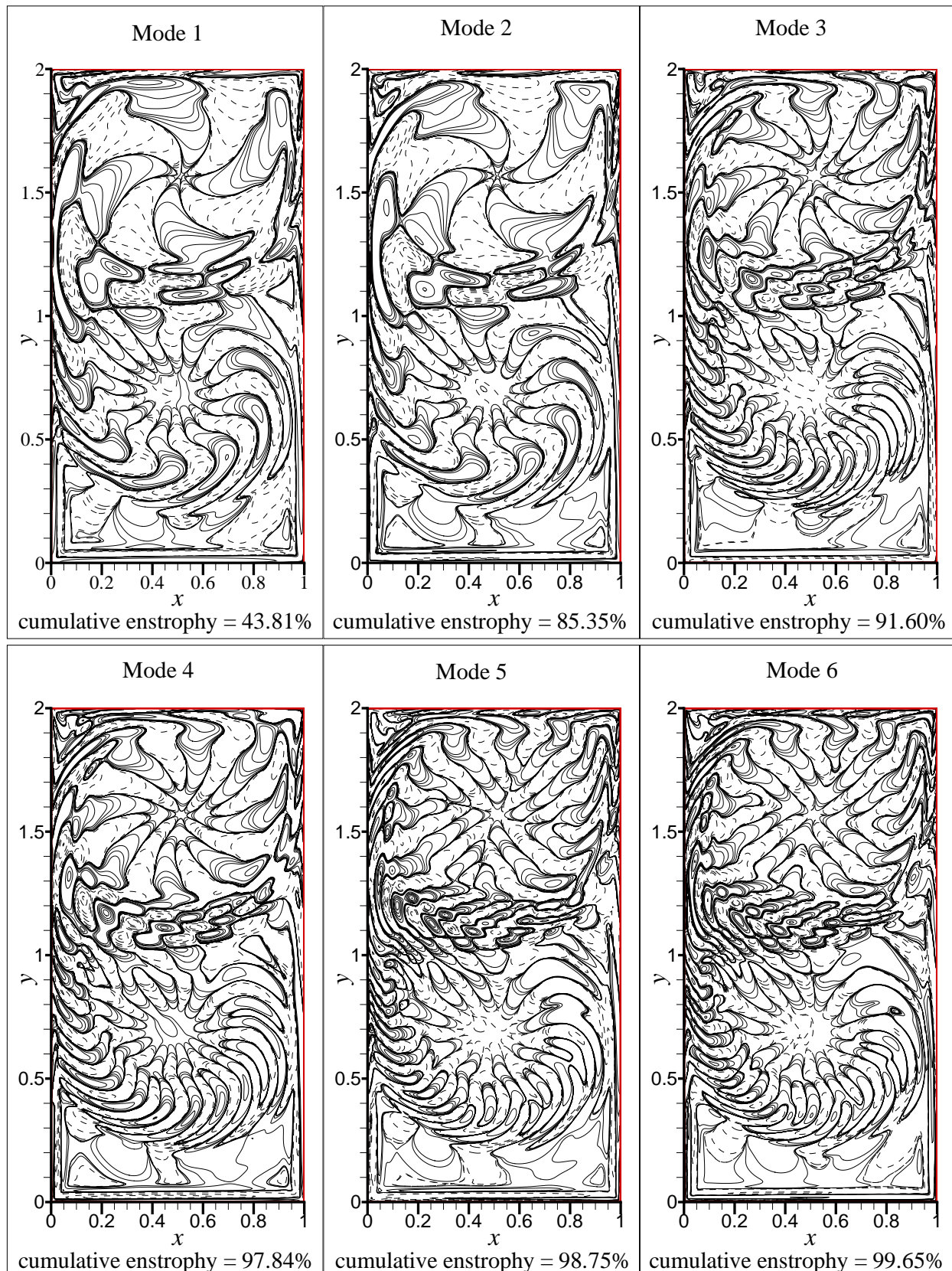


Figure 17 First six eigenfunctions for rectangular (with depth to width ratio of 2:1) LDC flow for  $Re = 6000$  shown. The POD is carried out from  $t = 1287$  to  $t = 1487$ .